SYNTHETIC STRATEGIES FOR GENERATING INORGANIC NANOPARTICLES WITH OPTICAL, CATALYTIC, AND BIOLOGICAL IMPORTANCE

By

KACHCHAKADUGE DESHANI GIHANTHIKA FERNANDO

Bachelor of Science in Chemistry
University of Kelaniya
Kelaniya, Sri Lanka
2009

Submitted to the Faculty of the
Graduate College of the
Oklahoma State University
in partial fulfillment of
the requirements for
the Degree of
DOCTOR OF PHILOSOPHY
December, 2017

SYNTHETIC STRATEGIES FOR GENERATING INORGANIC NANOPARTICLES WITH OPTICAL, CATALYTIC, AND BIOLOGICAL IMPORTANCE

Dissertation Approved:

Dr. Yolanda Vasquez

Dissertation Adviser

Dr. Allen Apblett

Dr. Ziad El Rassi

Dr. Jeffery White

Dr. Heather Fahlenkamp

ACKNOWLEDGEMENTS

I would like to humbly thank “Almighty God” for providing me with blessing and strength to accomplish this work and for guiding me in good times and bad.

I would like to thank my graduate advisor, Dr. Yolanda Vasquez for her support. I extend my sincere thanks to my committee members, Dr. Allen Apblett, Dr. Ziad El Rassi, Dr. Jeffery White and Dr. Heather Fahlenkamp for their positive feedback and support.

I also wish to thank my friends, colleagues, faculty members and all the staff members in the department of Chemistry for making my time at Oklahoma State University a great experience. Additionally, I also want to thank the staff members at OSU microscopy center for their help.

Finally, I would like to thank my loving parents for their sacrifices, encouragements and blessings and my husband and daughter for all their love and patience. I would also like to thank my loving grandmother and entire family for all their blessings and love.

Name: KACHCHAKADUGE DESHANI GIHANTHIKA FERNANDO

Date of Degree: DECEMBER, 2017

Title of Study: SYNTHETIC STRATEGIES FOR GENERATING INORGANIC NANOPARTICLES WITH OPTICAL, CATALYTIC, AND BIOLOGICAL IMPORTANCE

Major Field: CHEMISTRY

Abstract:

Solution-based synthesis methods have been widely used to synthesize nanocrystals as it provides control over the size and shape. As a result of the rapid success of the solution based synthesis methods, new applications have been found for some metallic nanoparticles (e.g. gold nanorods), and metal chalcogenides (e.g.CdS) while showing promising properties. In addition, the synthesis of nanoparticles has extended beyond the metal nanoparticles and metal chalcogenides, with increased attention towards synthesizing metal phosphides due to their potential applications in the semiconductor industry, as magnetic devices, and as catalysts. In the following chapters, synthesis of nanostructures from three different classes of material (gold nanorods, gold phosphides, and cadmium sulfides) will be presented using solution-based approaches while further studying their properties.

TABLE OF CONTENTS

Chapter Page

I. SYNTHETIC STRATEGIES FOR GENERATING INORGANIC NANOPARTICLES WITH OPTICAL, CATALYTIC, AND BIOLOGICAL IMPORTANCE 1

Introduction.....1

II. CELLULAR UPTAKE OF DIFFERENT ASPECT RATIOS OF GOLD NANORODS 5

Introduction.....5
Experimental Section.....8
Results and Discussion 16
Conclusion 30

III. SYNTHESIS OF METASTABLE PHASE OF GOLD PHOSPHIDE 31

Introduction.....31
Experimental Section.....33
Results and Discussion 36
Conclusion 53

IV. CADMIUM SULFIDE DEPOSITION ON MICROSTRUCTURED SURFACES BY CHEMICAL BATH DEPOSITION 55

Introduction.....55
Experimental Section.....57
Results and Discussion 58
Conclusion 70

V. SUMMARY AND CONCLUSION.....71

REFERENCES 74

LIST OF TABLES

Table Page

2.1. Mass of Au per nanorod for all four aspect ratios calculated using ICP-AES and TEM data 12

4.1. Average absorption onset values, band gaps determined using UV-Vis absorption spectra of CdS thin films deposited at pH 8 and pH 10.....67

LIST OF FIGURES

Figure Page

2.1. Characterization of gold nanorods 17

2.2. UV-Vis-NIR absorption spectra and ATR-FTIR spectra of Au nanorods before and after functionalizing with mPEG 18

2.3. Zeta potentials of CTAB-coated Au nanorods and mPEG-coated Au nanorods..20

2.4. Media interaction studies with CTAB and mPEG-coated Au nanorods.....21

2.5. Cell viability studies of HeLa cell after incubating with the CTAB coated Au nanorods, mPEG coated Au nanorods and supernatant of different aspect ratios 23

2.6. Cell viability studies of HeLa cell after incubating with CTAB, $AgNO_3$, and hydroquinone 25

2.7. Cellular uptake studies conducted by using ICP-AES after incubating HeLa cell for 3 h, 6 h,10 h and 24 h with different aspect ratios of Au nanorods having CTAB and TEM images of HeLa cells treated with CTAB functionalized Au nanorods (80 pM) for 24 h 27

2.8. Cellular uptake with mPEG coated Au nanorods (80 pM) for 10 h to 48 h and comparison between the cell viability of HeLa cells after 24 h treatment with 80 pM of CTAB coated Au nanorods and mPEG coated Au nanorods 28

2.9. Magnified TEM images of HeLa cells treated with mPEG coated Au nanorods (80 pM) for 24 h 29

3.1. Characterization of surface functionalized gold nanorods 37

3.2. Powder X-ray diffraction patterns of nanocrystal products formed by reacting gold nanorods functionalized with 1-dodecanethiol with a 1:1 TOP/TOPO ratio 39

Figure Page

3.3. Powder X-ray diffraction patterns of nanocrystal products formed by reacting gold nanorods functionalized with 1-dodecanethiol with a 2:1 TOP/TOPO ratio 40

3.4. Powder X-ray diffraction patterns of nanocrystal products formed by reacting gold nanorods functionalized with CTAB with a 1:1 TOP/TOPO ratio 41

3.5. Powder X-ray diffraction patterns of nanocrystal products formed by reacting gold nanorods functionalized with CTAB with a 2:1 TOP/TOPO ratio 42

3.6. Time evolution of the morphology of gold nanorods functionalized with 1-dodecanethiol after reacting in a 1:1 TOP/TOPO ratio 43

3.7. TEM images of the nanoparticles synthesized from the reaction of gold nanorods stabilized with1-dodecanethiol and TOP/TOPO in a 2:1 ratio 45

3.8. TEM images of the nanoparticles synthesized from the reaction of gold nanorods stabilized with CTAB and TOP/TOPO in a 1:1 ratio. 48

3.9. HRTEM images of Au_2P_3 formed by reacting CTAB stabilized gold nanorods with TOP/TOPO at 360 ˚C.....49

3.10. TEM images of nanoparticles synthesized by reacting CTAB stabilized gold nanorods with a 2:1 TOP/TOPO ratio 50

3.11. Polarization data for three Au_2P_3 electrodes in 0.1 M $HClO_4$ acid with polycrystalline gold and platinum for comparison 52

3.12. FTIR spectra of pure TOP, pure TOPO, Au_2P_3 prepared by reacting CTAB coated gold nanorods and TOP/TOPO 2:1 ratio 53

4.1. Time – dependent X-ray diffraction patterns of hexagonal (WZ-type) CdS synthesized by CBD at pH = 8.....60

4.2. Time – dependent X-ray diffraction patterns of CdS synthesized by CBD at pH = 10 61

4.3. SEM images of CdS thin films deposited on a hexagonal array of epoxy micropillars synthesized by CBD at pH = 10.....64

Figure Page

4.4. SEM images of CdS thin films deposited on a hexagonal array of epoxy micropillars synthesized by CBD at pH = 8 65

4.5. Representative UV-Vis and photoluminescence spectra of CdS thin films deposited at pH 8 and pH 10 67

4.6. SEM images of CdS thin films deposited on an Au/Pd coated hexagonal array of epoxy micropillars synthesized by CBD at pH 10 for 180 min 69

4.7. SEM images of CdS deposited at pH 10 on 1-dodecanethiol functionalized, Au/Pd coated epoxy substrates having micropillars 69

LIST OF ACRONYMS

CTAB: Cetyltrimethylammonium bromide/ Hexadecyltrimethylammonium bromide

mPEG: O-[2-(3-Mercaptopropionylamino)ethyl]- O′-methylpolyethylene glycol

LSPR: Localized Surface Plasmon Resonance

AR: Aspect Ratio

TEM: Transmission Electron Microscopy

ATR-FTIR: Attenuated Total Reflection-Fourier Transform Infrared

ICP-AES: Inductively Coupled Plasma- Atomic Emission Spectroscopy

DCS: Donor Calf Serum

PBS: Phosphate-Buffered Saline

SDS-PAGE: Sodium Dodecyl Sulfate Polyacrylamide Gel Electrophoresis

TOP: tri-*n*-octylphosphine

TOPO: tri-*n*-octylphosphine oxide

DDT: l-dodecanethiol

HER: Hydrogen Evolution Reaction

REH: Reversible Hydrogen Electrode

HOR: Hydrogen Oxidation Reaction

XRD: X-ray Diffraction

CBD: Chemical Bath Deposition

PDMS: Poly (dimethyl)siloxane

WZ: Wurtzite

ZB: Zinc-blend

SEM: Scanning Electron Microscopy

EDX: Energy Dispersive X-ray Spectroscopy

HRTEM: High-Resolution Transmission Electron Microscopy

CHAPTER I

SYNTHETIC STRATEGIES FOR GENERATING INORGANIC NANOPARTICLES WITH OPTICAL, CATALYTIC, AND BIOLOGICAL IMPORTANCE

1.1 INTRODUCTION

Nanotechnology deals with materials at the nano-scale that demonstrate new chemical and physical properties different from than their bulk counterparts by virtue of the high surface to volume ratio and quantum confinement.[1-3] Nanoscale materials can be synthesized following two different approaches; the chemical approach and the physical approach. Nature uses small building blocks to create highly ordered nano-scaled structures with distinct shapes and functions by following the chemical method, which is known as the "bottom-up" approach.[4,5] This method involves the building of nanoparticles starting from atoms and molecules. Nanoscale materials can also be synthesized using the "top-down" method that involves the reduction of the size of solid using techniques such as grinding and lithography.[6] Compared to the top-down method, bottom-up approach has the advantage of producing nanoparticles with less defects, high purity, and homogeneous chemical composition.[6] The synthesis of nanoparticles using solution-based

methods can be classified into the "bottom-up" method where nanocrystals with controlled shape and size can be accessed.[1,7] Some of the most widely used solution-based chemical approaches employed in the synthesis of nanocrystals include thermal decomposition of organometallic complexes,[8] solvothermal chemical synthesis protocols,[9,10] reduction of metal salts,[11,12] and precipitation techniques.[13,14] Solution based synthesis protocols generally require the use of surface stabilizers to facilitate shape control by acting as structure directing agents while providing tight control over the size, shape, and dispersibility.[15,16] In the following chapters, synthesis of nanostructures from three different classes of material (metals, phosphides, and sulfides) will be presented using chemical synthetic methods such as solution-based approaches while further studying their properties.

As a result of the success of the solution based synthesis methods, new applications have been found for some metallic nanoparticles (Au, Ag, Ni, Co). Particularly, anisotropic nanoparticles such as gold nanorods have been used in a wide range of applications in photothermal therapy, biosensing, bioimaging and drug delivery.[16-19] The seed-mediated method is the most commonly used synthesis protocol to access a variety aspect ratios of gold nanorods and utilizes CTAB as the surface capping agent. Many researchers have studied the cellular uptake and cytotoxicity of rod- shaped Au nanoparticles:[20-22] however, the results of some of these studies are in conflict with each other. Even though the higher aspect ratios have promising photothermal properties such as a surface plasmon peak in the near-IR region and enhanced fluorescence properties,[16] no current literature reports have examined the cellular uptake and cytotoxicity of Au nanorods beyond the aspect ratio 7. Chapter II focuses on the synthesis and cellular uptake of four different aspect ratios of gold nanorods ranging from 2.6 to 11.5, while also considering the influence of other parameters such as the surface stabilizer, effect of the supernatant, and serum proteins present in the medium. Cell viability studies were conducted with all four aspect ratios of CTAB functionalized gold nanorods at different time intervals and results have been compared with thiolated poly (ethylene glycol) (mPEG) stabilized

gold nanorods. Furthermore, cellular uptake studies with different aspect ratios of gold nanorods were performed using inductive-coupled plasma analysis and transmission electron microscopy.

Nano-scale metal chalcogenides synthesized chemically have also shown some promising applications in the semiconductor industry with potential applications in solar cells, sensors, optoelectronic devices, and light emitting diodes.[23,24] Among the many types of metal chalcogenides, CdS has been one of the most widely studied semiconductor material due to its applications in solar cells.[25] Even though several methods have been developed to synthesize nanoparticles and thin films of CdS, obtaining high quality, phase pure CdS thin films and nanostructures at low temperatures has been a challenge with variables such as pH, temperature, and type of substrate affecting the quality of the films.[26-28] Chapter IV highlights the formation of thin films and nanostructures of CdS by chemical bath deposition and it also emphasizes the importance of pH in determining the purity of the crystal phase of CdS. The effect of substrate topography or roughness on the morphology and crystal structure of CdS were evaluated by depositing CdS onto flat epoxy, glass slides, and epoxy having micropillar arrays. Time studies were conducted at two different pH conditions (pH 8 and pH 10) in order to identify the effect of pH on the morphology and crystal structure of CdS. The optical properties of the CdS films were studied using UV-Vis specrophotometer. Studies were also undertaken to determine whether CdS nanowires could be nucleated on the epoxy micropillar arrays using chemical bath deposition.

In the past few decades, the synthesis of nanoparticles has extended beyond the metal nanoparticle and metal chalcogenides, with the increased attention towards synthesizing metal phosphides due to their potential applications in the semiconductor industry, as magnetic devices, and as catalysts.[29-36] Several transition metal phosphides such as NiP, CoP and FeP have been synthesized by diffusing elemental phosphorous into metallic nanoparticle precursors. These materials have shown excellent catalytic activity towards the hydrogen evolution reaction (HER) at the nanoscale.[37-44] Since the synthesis of phase pure gold phosphide, Au_2P_3, is a challenge because of the use of harsh

reaction conditions such as high temperatures and high pressure, the catalytic activity and other physical properties of this material are not well known. Therefore, there was a need to develop a chemical synthesis protocol that uses mild reaction conditions to obtain pure metastable gold phosphide nanocrystals to further study the properties of the material. Chapter III discusses the synthesis and catalytic activity of gold phosphide nanoparticles synthesized by using gold nanorods as a metal template while reacting with tri-*n*-octylphosphine (phosphorous source). The goal of this work was to examine the effect of capping agent and the morphology of the metal nanoparticle precursors on determining reactivity and how this affects the overall purity of the phase. From the results, it is apparent that the surface capping ligand of the precursor gold nanorod templates can determine the purity of the metastable gold phosphide phase, the extent to which it will form. Furthermore, the phase pure gold phosphides also displayed higher catalytic activity for the hydrogen evolution reaction compared to polycrystalline gold.

CHAPTER II

CELLULAR UPTAKE OF DIFFERENT ASPECT RATIOS OF GOLD NANORODS

2.1 INTRODUCTION

Gold nanorods have been studied extensively in past several years due to their unique optical properties which make them widely useful including as photonic devices and biomedical applications.[44] When gold nanoparticles interact with incident light, excitation of the conduction band electrons creates an oscillating dipole moment which is known as Localized Surface Plasmon Resonance (LSPR).[44,45] Due to the anisotropic shape of gold nanorods, two dipoles are created by interacting with light; a transverse peak that results from the short axis that can be observed in the visible region around 520 nm and the longitudinal peak from the long axis. The transverse peak is insensitive to the aspect ratio of gold nanorods, but the longitudinal peak shifts significantly from the visible to the near-infrared (NIR) region with the increasing length/width ratio or aspect ratio of the nanorod.[45] This change in the longitudinal peak is particularly advantageous for biological applications such as drug delivery and photothermal therapy, since light penetration is maximum and less harmful in the NIR region.[46,47] Furthermore, the sensitivity of the SPR band towards the local environment makes gold nanorods desirable for sensing

applications.[18] The strong scattering near the surface plasmon wavelength makes them suitable for biomedical imaging as well.[48]

Several methods have been reported for the synthesis of gold nanorods such as template-assisted synthesis,[49] electrochemical synthesis,[50] and wet chemical synthesis methods.[19,4546,51-53] Among the many synthesis protocols, the seed-mediated method has been used extensively to produce nanorods due to its reproducibility, high yields, purity, and ability to access a wide range of aspect ratios.[50,53] Despite the extensive work in applying gold nanorods in biomedical applications, there are many drawbacks in the effective delivery of these materials to the affected or diseased tissue. On average, only 0.7% of the nanoparticle dose is actually delivered to the target area such as a tumor. Particle aggregation, flow, diffusion, protein adsorption, and phagocytosis sequestration are among the many barriers that continue to impede the effective use of nanoparticles, which makes it imperative to understand the interactions of gold nanorods with biological systems.[54] In recent years, a number of research studies have been devoted to identifying how the surface ligands, size, and charge of gold nanorods affect cellular endocytosis, exocytosis, localization, and cellular toxicity.[20-22,47,55-57] Even with the large number of studies, a firm conclusion on the effect of different aspect ratios of gold nanorods on cellular endocytosis has yet to be made. For example, Chan et al.[22,57] observed a decrease in the cellular uptake of hexadecyltrimethylammonium bromide (CTAB) functionalized gold nanorods with increasing aspect ratio (1 to 6) with the HeLa cancer cell line. However, Ghandehari and co-workers[58] showed an increase in the cellular uptake for poly (ethylene glycol) functionalized Au nanorods (with aspect ratio 3.5 & 4.5) compared to the aspect ratio 1 in prostate cancer cells. In contrast, Choi et al.[21] found a lower uptake of poly (ethylene glycol) coated Au nanorods for higher aspect ratio (aspect ratio 7) compared to the smaller ones (1, 2 & 4) when used with mouse endothelial cells. Choi et al. also observed a higher cell uptake specifically for aspect ratio 2 compared to the other aspect ratios (1, 4 & 7) when the surface of the Au nanorods was functionalized with a

DNA oligonucleotide.[21] Most of these cellular uptake and cytotoxicity studies used Au nanorods with an aspect ratio of 7 or less. Even though the higher aspect ratios (length > 200 nm) shown enhanced fluorescence, photoluminescence and photothermal properties due to the longitudinal surface plasmon oscillations,[45] and which can be more useful in biological imaging and photothermal therapy. To the best of our knowledge, no literature reports have been reported on cellular uptake and cytotoxicity of Au nanorods with an aspect ratio as high as 11.5, which we report here. We systematically study the effect of aspect ratio of Au nanorods on cell viability and cellular uptake with nanorods ranging in aspect ratios from 2.6 to 11.5 while also considering the influence of other parameters such as the surface stabilizer, the effect of supernatant and serum proteins present in the medium.

Here, four aspect ratios of Au nanorods were synthesized including 2.6, 3.2, 5.4 and 11.5 using a seed-mediated growth protocol with CTAB as the surface capping agent. Furthermore, to identify the effect of surface functional group on cellular interaction, the Au nanorods were subsequently functionalized with a thiolated poly (ethylene glycol) (mPEG) molecule. Cellular uptake and toxicity studies were carried out with CTAB and mPEG functionalized Au nanorods using HeLa cells as the model cell line. Our results show higher uptake for CTAB functionalized Au nanorods compared to mPEG. Importantly, Au nanorods of aspect ratio of 11.5 showed the highest uptake when CTAB was used as a surface capping ligand compared to mPEG coated Au nanorods and shorter aspect ratios. These high aspect ratio Au nanorods could have potential applications in photothermal therapy and imaging.

2.2 EXPERIMENTAL SECTION

2.2.1 Chemicals

Gold (III) chloride trihydrate (99.99%), cetyltrimethylammonium bromide (CTAB, 99%), sodium borohydride (99%), L-ascorbic acid (99%), sodium hydroxide (97%), sodium citrate (99%), hydroquinone (99%), silver nitrate (99%), and O-[2-(3-Mercaptopropionylamino)ethyl]-O′-methylpolyethylene glycol (MW = 5000 g/mol, 99.99%) were purchased from Sigma-Aldrich (Missouri, USA). All chemicals were used without further purification, and all solutions, except those of gold and CTAB were prepared freshly using deionized water (18.2 MΩ). Dedicated glassware was cleaned before each reaction with aqua regia (CAUTION: Corrosive) and then rinsed with deionized water. Standard solution of gold (1000 mg/L in 3% HCl) was purchased from RICCA chemical company. Analytical grade hydrochloric and nitric acid were purchased from Thermo Fisher Scientific.

2.2.2 Seed-Mediated Growth of Gold Nanorods

Synthesis of gold nanorods with aspect ratio (AR) of 2.6

AR 2.6-CTAB stabilized Au nanorods were synthesized by seed-mediated growth method as described elsewhere[53] with minor modifications. Briefly, the seed solution consisted of CTAB (0.20 M, 5.00 mL) and $HAuCl_4 \cdot 3H_2O$ (0.50 mM, 5.00 mL). $NaBH_4$ (0.010 M, 600 µL) was added to the CTAB and $HAuCl_4 \cdot 3H_2O$ solution, while vigorously stirring with a magnetic stir bar for 2 min. The seed solution was kept at 27 ˚C and used within 2 – 3 h. For the growth solution, CTAB (0.20 M, 5.00 mL) was mixed with $HAuCl_4 \cdot 3H_2O$ (1.0 mM, 5.00 mL). $AgNO_3$ (4.0 mM, 250 µL) was added to the growth solution. After gentle mixing of the solution, ascorbic acid (78.8 mM, 70 µL) was added to the growth solution and swirled until it became colorless.

Finally, 12 μL of the seed solution was added to the growth solution and kept at 27 ˚C overnight. The colloidal suspension was centrifuged twice at 8,000 rpm for 30 min. and stored in water.

Synthesis of gold nanorods with AR of 3.2

Gold nanorods with an AR of 3.2 were synthesized by a seed mediated method as described elsewhere.[51] In the seed solution, CTAB (0.10 M, 7.50 mL) was mixed with $HAuCl_4 \cdot 3H_2O$ (0.01 M, 250 μL). Then, $NaBH_4$ (0.01 M, 600 μL) was added while stirring. After vigorous stirring, the solution was kept at 27 ˚C and used within 2 h- 3 h. The growth solution was made by mixing CTAB (0.10 M, 4.75 mL) with $HAuCl_4 \cdot 3H_2O$ (0.010 M, 200 μL). $AgNO_3$ (0.010 M, 30 μL) was added to this mixture. After gently mixing the solution, ascorbic acid (0.10 M, 32 μL) was added and swirled until the solution became colorless. Finally, 10 μL of the seed solution was added to the growth solution and kept at 27 ˚C overnight. The reaction was centrifuged twice at 8,000 rpm for 30 min. and stored in water.

Synthesis of gold nanorods with AR of 5.4

Au nanorods with an AR of 5.4 were synthesized by a seed mediated method as described elsewhere[59] with minor modifications. In the seed solution, CTAB (0.20 M, 5.00 mL) was mixed with $HAuCl_4 \cdot 3H_2O$ (1.0 mM, 5.00 mL). Then, $NaBH_4$ (0.010 M, 460 μL) in 0.010 M NaOH was added to the seed solution while stirring with a magnetic stir bar for 2 min. The solution was kept at 27 ˚C and used within 2 h- 3 h. The growth solution consisted of CTAB (0.20 M, 5.00 mL) and $HAuCl_4 \cdot 3H_2O$ (1.0 mM, 5.00 mL). $AgNO_3$ (0.10 M, 35 μL) was added to the growth solution. After vigorous mixing, hydroquinone (0.10 M, 500 μL) was added and swirled until the solution became clear and colorless. Finally, the seed solution (160 μL) was added to the growth solution, mixed thoroughly, and allowed to age overnight at 27 ˚C. The nanorods were isolated by centrifugation (13,000 rpm, 10 min.) and dispersed in water.

Synthesis of gold nanorods with AR of 11.5

Au nanorods were synthesized by a three-step seed mediated growth process as described elsewhere.[60] The seed solution included $HAuCl_4 \cdot 3H_2O$ (0.010 M, 0.50 mL) and sodium citrate (0.010 M, 0.50 mL) in 18.00 mL of water. $NaBH_4$ (0.10 M, 500 μL) was then added while stirring. The solution was aged at room temperature for 2 h without stirring and used immediately. Three vials were labeled A, B, and C. Growth solutions A and B consisted of 9.00 mL of 0.1 M CTAB, $HAuCl_4 \cdot 3H_2O$ (0.010 M, 0.25 mL), ascorbic acid (0.10 M, 50 μL), and NaOH (0.10 M, 50.0 μL). Growth solution C was prepared with CTAB (0.10 M, 90.0 mL), $HAuCl_4 \cdot 3H_2O$ (0.010 M, 2.50 mL), ascorbic acid (0.10 M, 500 μL), and NaOH (0.10 M, 500 μL). Finally, 1.00 mL of the seed solution was added to growth solution A. After shaking vigorously for 3-5 s, 1.00 mL of solution A was added to solution B. Solution B was shaken vigorously for 3-5 s, and the entire volume was transferred into growth solution C. This solution was aged overnight at 27 ˚C. Gold nanorods were separated using sedimentation. Further purification was carried out using 0.10 M CTAB to isolate a higher yield of gold nanorods. Finally, the gold nanorods were isolated by centrifugation (twice at 1,500 rpm for 20 min.) and dispersed in 1.0 mL of water. To obtain a higher yield of nanorods for the cell experiments, this synthesis procedure was scaled up by 4.

2.2.3 Determination of Gold Nanorod Concentration

Concentration of Au nanorods was determined by using a literature reported method with further modifications.[61] Briefly, by using the images taken from TEM, we measured the dimensions of each aspect ratio and calculated the volume of a nanorod. For AR 11.5 volume was determined by using equation (1) assuming the cylindrical middle (h) having 2 spherical caps with the height (a) and radius (r) as observed in TEM. Since no spherical caps were observed clearly for AR 2.6, AR 3.2 and AR 5.4, volume was determined only by considering the

cylindrical middle with length (h). Assuming atom density of gold (D) (59 atoms/ nm^3)[61] with the face-centered cubic crystal structure, the mass of Au per nanorod was calculated for each aspect ratio (equation 2) as shown in Table 2.1. By using the mass of Au per nanorod calculated previously and by analyzing the Au atom content of all four aspect ratios separately using inductively coupled plasma- atomic emission spectroscopy (ICP-AES), gold nanorod concentration was determined by using equation (3).

$$\text{Volume (V)} = \left(\frac{\pi}{3}\right) a\,(3r^2 + a^2) + (\pi r^2 h) \qquad \text{Equation (1)}$$

$$\text{Mass of Au per nanorod (g/nanorod)} = V \times D \times 197\ \text{gmol}^{-1} / (6.022 \times 10^{23}) \qquad \text{Equation (2)}$$

$$\text{Gold nanorod concentration (nanorods/L)} = \frac{\text{Au atom concentration from ICP (g/L)}}{\text{Mass of Au per nanorod (g/nanorod)}} \qquad \text{Equation (3)}$$

After calculating the gold nanorod concentration, a calibration curves were prepared by varying the concentration of Au nanorods and by observing the absorbance at λ_{max} for three shorter rods (AR 2.6, AR 3.2 and AR 5.4) and at 520 nm for AR 11.5 by referring to a previous protocol.[62] Before every experiment concentration of Au nanorod in each sample was determined using the calibration plots developed previously.

Table 2.1. Mass of Au per nanorod for all four aspect ratios calculated using ICP-AES and TEM data

Aspect Ratio	Mass of Au per nanorod (g/nanorod)
AR 2.6	7.00×10^{-16}
AR 3.2	2.36×10^{-16}
AR 5.4	1.10×10^{-15}
AR 11.5	2.58×10^{-15}

2.2.4 Preparation of mPEG-Coated Gold Nanorods

Ligand exchange was carried out by making minor modifications to the traditional mPEG functionalization protocols.[48,63] For the ligand exchange of nanorods of aspect ratios 2.6, 3.2, and 5.4, a mole ratio of 1: 1×10^6 between CTAB functionalized gold nanorods and mPEG (*o*-[2-(3-mercaptopropionylamino)ethyl]-*o′*-methylpolyethylene glycol) was utilized. For nanorods of aspect ratio 11.5, a mole ratio of 1: 2×10^6 of gold nanorods (CTAB) to mPEG was used for ligand exchange. After determining the concentration of Au nanorods in each sample, pre-determined amounts of mPEG were added to the purified Au nanorod having CTAB (2 mL) on the surface. This was stirred with a magnetic stir bar in distilled water for 24 h at room temperature, washed twice with deionized water, and centrifuged to separate mPEG-coated gold nanorods.

2.2.5 Characterization of Gold Nanorods

UV-Vis-NIR absorption spectra of Au nanorods were collected using a Beckman Coulter DU530 spectrophotometer and Cary 5000 UV-Vis-NIR spectrophotometer. Transmission

electron microscopy (TEM) images of the nanorods, taken on a JEOL-JEM 2100 TEM (200 kV), were used to determine the size distribution of approximately 250 Au nanorods with the aid of ImageJ 1.47vsoftware (Wayne Rasband National Institutes of Health, USA). The zeta potential of gold nanorods was measured using dynamic light scattering instrument (Zetasizer Nano ZS90, Malvern Instruments) at a temperature of 25 ˚C, to determine potential at the boundary of the electrical double layer of the nanorods. ATR-FTIR spectroscopy was performed on Au nanorods to identify surface ligands and ensure complete exchange.

2.2.6 Cell Studies

HeLa cells were cultured in complete RMPI- 1640 medium (Gibco, Life technologies) containing 10% (v/v) donor calf serum (DCS) (Hyclone, GE Healthcare Life Sciences) and 1% (v/v) penicillin-streptomycin (Gibco, Life technologies) in a CO_2 incubator (Symphony 5.3A, VWR) at 37 ˚C and 5% CO_2 (Air gas). Frozen HeLa cells (1×10^6 cells/mL, 1.00 mL) were expanded in a T75 culture flask (Nunclone) with complete media. Once the cells reached 80% confluency, cells were subcultured in T175 culture flasks (Nunclone) having complete media and used for further cell studies. The cell viability assay was performed using the live/dead viability assay kit (Molecular Probes) from Invitrogen Detection Technologies.

2.2.7 Cell Viability Studies with Gold Nanorods

Cell viability studies with four different aspect ratios were performed using live/dead cell viability assay kit. First, cells (5×10^4 cells/cm^2) were seeded in 96 multiwell plates and incubated for 20 h. After removing the spent medium, cells were washed twice with phosphate-buffered saline solution (PBS). Complete media containing CTAB stabilized Au nanorods (80 pM, 100 μL) was then added to each well. Control experiments consisted of culturing HeLa cells without gold nanorods. Cells were incubated for time intervals of 3 h, 6 h, 10 h and 24 h. Then the cells were washed twice with PBS and 100 μL of the live/dead reagent solution was added to

each well. The cells were then observed using fluorescence microscopy (Olympus IX83, inverted) using GFP and RFP filters. ImageJ 1.47v software (Wayne Rasband National Institutes of Health, USA) was used for image analysis and cell counts. Experiments were performed in triplicates. Cell viability studies were also conducted with mPEG coated gold nanorods only at an incubation period of 24 h following the same protocol. Cell viability studies were not conducted at shorter time points with mPEG stabilized Au nanorods since there was no significant toxicity observed even at 24 h. Viability studies were also performed with the supernatant of the CTAB functionalized Au nanorods to determine whether toxicity was primarily a result of exposure to nanorods or to the supernatant.

2.2.8 Cellular Uptake Studies with Gold Nanorods

Quantification of Au uptake by HeLa cells was performed using inductively coupled plasma- atomic emission spectroscopy (ICP-AES, SPECTRO). For these experiments, cells at a seeding density of 5×10^4 cells/cm^2 were cultured in 6-well plates for 20 h. After removing media, cells were washed twice with PBS and treated with 2.00 mL of 80 pM Au nanorods (CTAB or mPEG functionalized) dispersed in RPMI media. The HeLa cells were incubated with CTAB functionalized Au nanorods for 3 h, 6 h, 10 h and 24 h for ICP-AES experiments. After incubating, the cells were washed twice with PBS, trypsinized, pelleted, and soaked in aqua regia (1.00 mL) overnight. Furthermore, the aqua regia solution was heated to 140 ˚C to completely dissolve the Au nanorods. These digested samples were dispersed in a matrix of 3% HCl (5.00 mL) to match with the matrix of standard solutions used in the preparation of calibration cure and the concentration of Au atoms in each sample was determined by ICP-AES. The concentration Au atoms (ppm) was converted to concentration of Au rods by calculating number of atoms per rod, which was estimated from the volume of an average Au nanorod assuming an atom density of 59 Au atoms/ nm^3.[61] ICP-AES experiments were performed in triplicates for each nanorod size and time point. For mPEG functionalized Au nanorods, ICP-AES measurements were performed

only at time points of 10 h, 24 h and 48 h since the Au concentrations did not change and HeLa cells did not readily uptake Au nanorods functionalized with mPEG. The concentration of nanorods was verified for each Au nanorod synthesis using ICP-AES and TEM images prior to exposing the cells to the particles.

2.2.9 Media Interaction Studies with Gold Nanorods

Zeta potential was used to determine the potential at the boundary of the electrical double layer after allowing Au nanorods having CTAB and mPEG on the surface to interact with media containing serum proteins. Au nanorods at a concentration of 80 pM were incubated in media having 10% DCS (37 ˚C for 24 h). After incubation, nanorods were separated by centrifugation, washed twice and dispersed in water and zeta potential was measured using dynamic light scattering instrument. To further study the changes in the surface plasmon resonance band, Au nanorods having CTAB and mPEG were analyzed using UV-Vis spectrophotometer after incubating in complete media for 24 h.

Protein binding on to the Au nanorod surface having CTAB and mPEG were also studied by sodium dodecyl sulfate polyacrylamide gel electrophoresis (SDS-PAGE). After incubating Au nanorods (80 pM, 3.00 mL) with different aspect ratios in complete media for 24 h having 10% DCS, each nanorod sample was centrifuged twice to remove unbound proteins present. Then, NaCl (1.00 M, 50 μM) was added into each Au nanorod sample and kept at room temperature overnight to separate the proteins bound to the surface of the Au nanorod. Supernatant of each Au nanorod sample was separated by centrifugation (8000 rpm, 30 min.), and mixed with a sample buffer (containing Tris HCl pH 6.8 (1 M), 30% w/v glycerol, 10% SDS, 0.12% bromophenol blue and dithiothreitol (0. 93 mg)) separately. This was heated (100 ˚C, 10 min.) and proteins adsorbed onto the surface were identified by electrophoresis with a gel containing 10% polyacrylamide.

2.2.10 Preparation of Cells for TEM Analysis

HeLa cells were cultured in a petri dish (100 mm) at a density of 5×10^4 cells/cm^2 and incubated for 20 h to promote cell attachment. After washing twice with PBS, the cells were treated with Au nanorods suspended in complete media (80 pM, 12.00 mL). These experiments were carried out with all four aspect ratios of both CTAB or mPEG functionalized Au nanorods. After incubating for 24 h at 37 ˚C, cells were washed twice with PBS, trypsinized, and pelleted by centrifugation. Cells were then fixed for 2 h in 2% glutaraldehyde (pH 7.0), washed three times with cacodylate buffer (0.2 M) for 15 min., and stained with OsO_4 (1%) dissolved in 0.2 M cacodylate buffer for 1 h. After washing the cells with cacodylate buffer, cells were serially dehydrated in ethanol and embedded in a Poly/Bed 812 resin. These polymer samples were sliced with an ultra-microtome (Sorvall MT 5000), and placed on carbon coated TEM grids for imaging.

2.3 RESULTS AND DISCUSSION

2.3.1 Preparation and Characterization of Gold Nanorods

Gold nanorods of four aspect ratios were synthesized by a seed-mediated method as described in the Experimental Section. Figures 2.1A and B show TEM images and UV-Vis-NIR spectroscopy of the CTAB functionalized Au nanorods. The aspect ratios (ARs) of the Au nanorods synthesized were 2.6 (±0.3), 3.2 (±0.2), 5.4 (±0.7) and 11.5 (±2) as shown in the representative TEM images in Figure 2.1A.

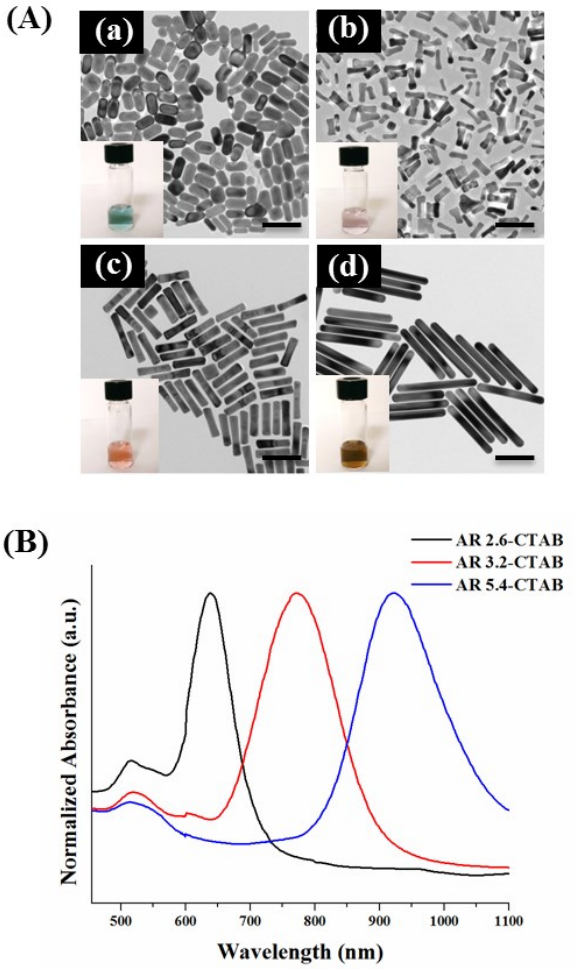

Figure 2.1. Characterization of gold nanorods. A) TEM images of CTAB functionalized Au nanorods synthesized by the seed-mediated method with aspect ratios of (a) 2.6, (b) 3.2, (c) 5.4, and (d) 11.5. B) Representative UV-Vis-NIR absorption spectra of the Au nanorods (CTAB-stabilized). Au nanorods exhibit transverse and longitudinal surface plasmon resonance (SPR) bands that correspond with the aspect ratio of the nanorods.

CTAB ligands on the as-synthesized Au nanorods were exchanged with mPEG (*o*-[2-(3-mercaptopropionylamino)ethyl]-*o′*-methylpolyethylene glycol). Ligand exchange was monitored using UV-Vis-NIR spectroscopy, FTIR, TEM, and by measuring the zeta potential of the Au nanorods. A 4 nm red shift was observed in all samples in the UV-Vis-NIR spectra of Au nanorods after mPEG functionalization (Figure 2.2A).[64] This suggests successful ligand exchange.[64] Moreover, the absence of additional peak broadening in the UV-Vis-NIR spectra, suggests that aggregation of the Au nanorods did not occur after functionalization with mPEG. This was further demonstrated by TEM analysis, where the particles do not aggregate and the sizes of the nanorods do not change after functionalization (Figure 2.2B inset).

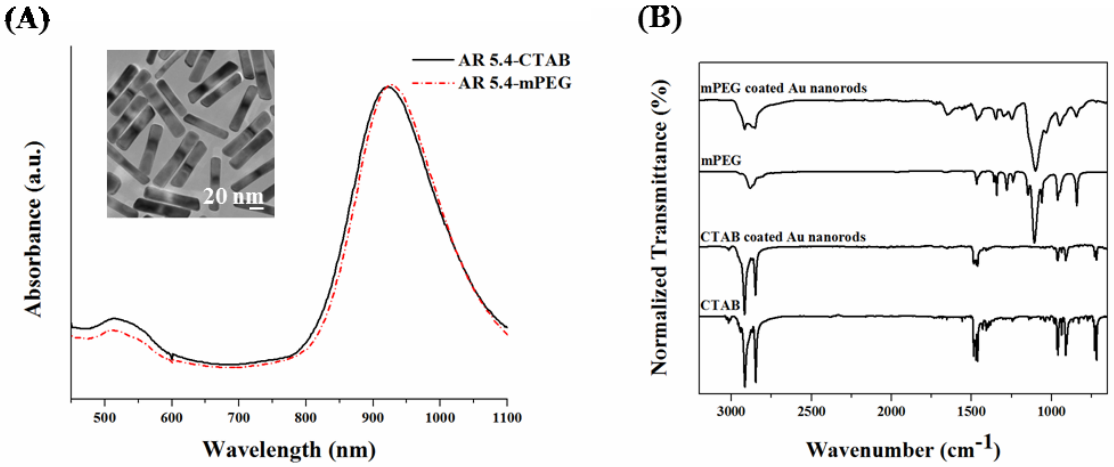

Figure 2.2. A) UV-Vis-NIR absorption spectra of AR 5.4-CTAB and AR 5.4-mPEG. Inset: TEM image of AR 5.4-mPEG Au nanorods. B) ATR-FTIR spectra of Au nanorods before and after functionalizing with mPEG. From top to bottom: mPEG coated AR 5.4 nanorods, neat mPEG, CTAB coated AR 5.4 nanorods and neat CTAB.

ATR-FTIR analysis was conducted on Au nanorod samples. Figure 2.2B shows representative ATR-FTIR spectra of neat CTAB, neat mPEG, and Au nanorods with an aspect ratio of 5.4 before and after ligand exchange. Au nanorods functionalized with mPEG showed a characteristic (C-O-C) stretching vibration at 1100 cm^{-1} together with other IR absorption peaks

characteristic of mPEG. The disappearance of the IR absorption peak at 3014 cm^{-1} corresponds to asymmetric $N(CH_3)_3^+$ stretching vibration mode of CTAB that verified the replacement of CTAB with mPEG on the surface of Au nanorods. Ligand exchange was further confirmed by measuring the zeta potential of the Au nanorods in water. CTAB functionalized Au nanorods exhibited a zeta potential of +40 mV while mPEG stabilized nanorods exhibited a negative zeta potential (Figure 2.3A). All these data indicated the successful functionalization of gold nanorods with mPEG for all aspect ratios. Observation of larger zeta potential value (> +30 mV) is indicative of the higher stability of the CTAB functionalized Au nanorods suspension in distilled water compared to the mPEG functionalized Au nanorods. Figure 2.3B shows the zeta potential of Au nanorods after incubation in full serum media for 24 h. Exposing CTAB functionalized Au nanorods to media resulted in a negative zeta potential (-20 mV) due to the adsorption of proteins.[20,65] Albumin, the most abundant protein in serum, is commonly adsorbed onto CTAB functionalized nanorods as identified and verified by prior studies.[17,65,66] The change in zeta potential from +40 mV (> +30 mV) to -20 mV (< -30 mV) also demonstrates the reduced stability of CTAB functionalized Au nanorods in full media after adsorption of proteins. The reduced stability of CTAB coated Au nanorods were further verified by the UV-Vis spectrophotometer with the change of the plasmon resonance band of AR 3.2 after 24 h of incubation in the presence of 10% DCS (Figure 2.4A). But in the case of mPEG coated Au nanorods no such change in plasmon resonance band was observed as shown in Figure 2.4B. Literature reports have shown that proteins are less likely to adsorb onto pegylated surfaces,[21,67,68] but we could not rule out the possibility of protein adsorption since the zeta potential did change on pegylated Au nanorods. Overall; pegylated Au nanorods retained a negative zeta potential. Gel electrophoresis studies conducted by extracting proteins on mPEG coated Au nanorods, also confirmed the presence of proteins on the surface as observed in CTAB coated Au nanorods (Figure 2.4C).

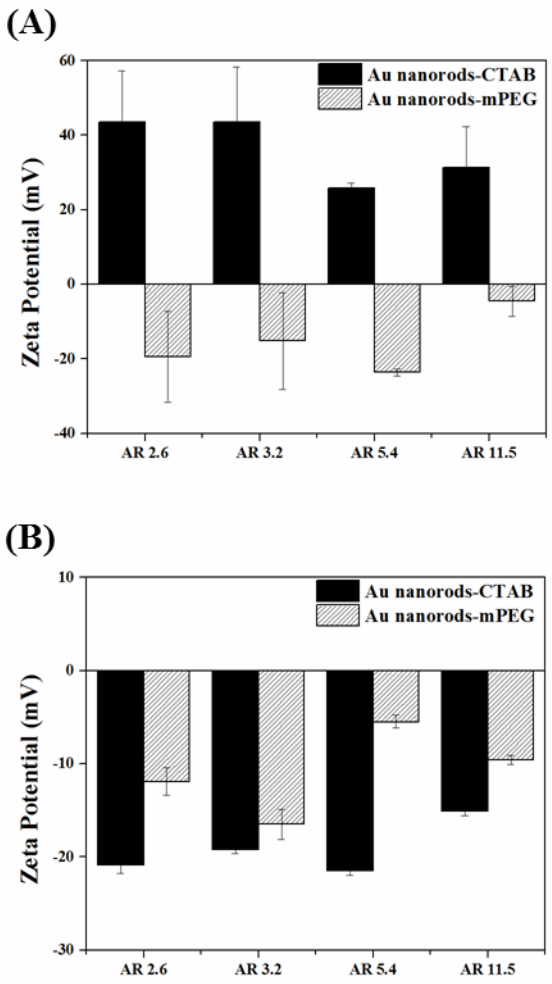

Figure 2.3. Zeta potentials of A) CTAB-coated Au nanorods and mPEG-coated Au nanorods in water after centrifugation and B) CTAB and mPEG coated nanorods dispersed in water after incubating in media for 24 h at 37 ˚C.

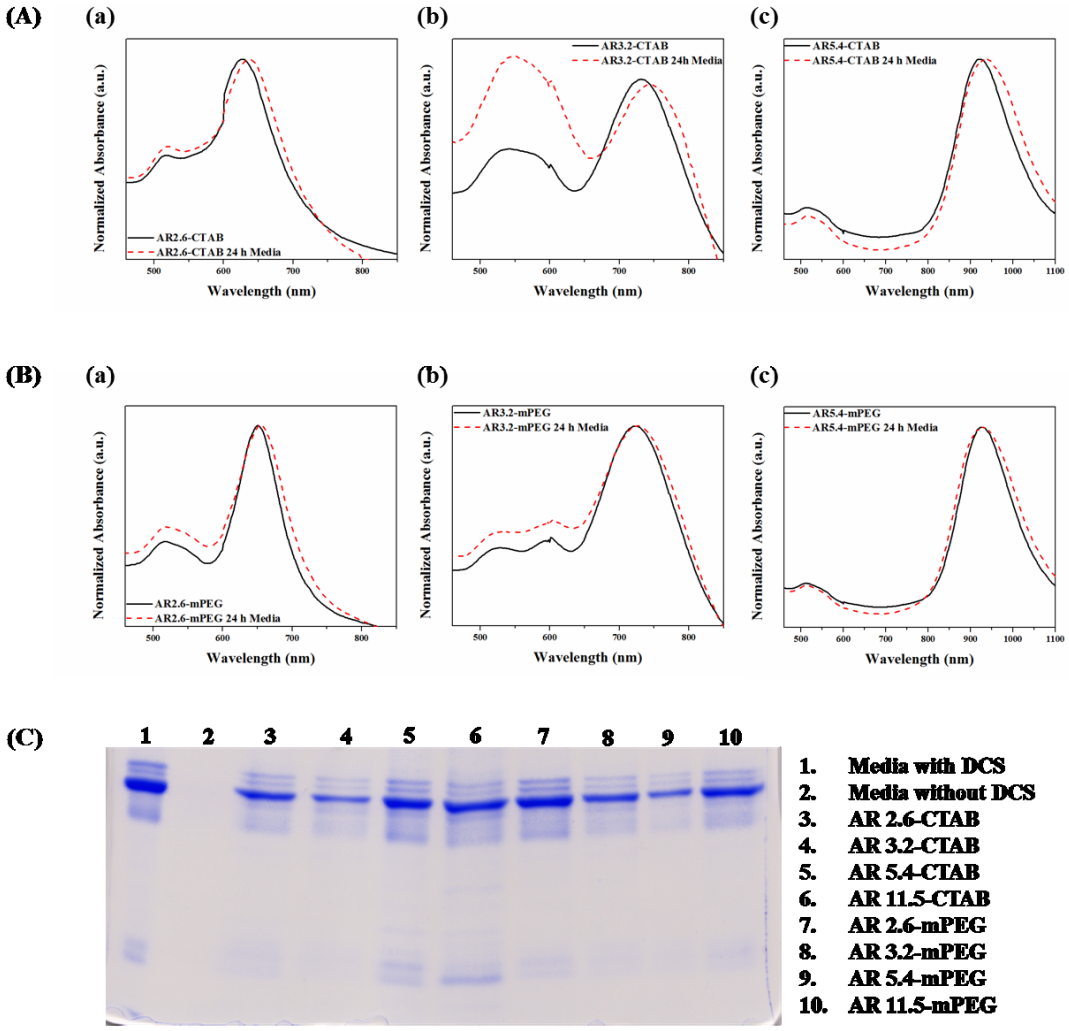

Figure 2.4. UV-Vis-NIR spectra of different aspect ratios of Au nanorods (80 pM) after incubating for 24 h in media having 10% DCS A) CTAB coated Au nanorods of (a) AR 2.6; (b) AR 3.2, & (c) AR 5.4, B) mPEG coated Au nanorods of (a) AR 2.6; (b) AR 3.2, & (c) AR 5.4. C) Bands observed in SDS-PAGE after incubating Au nanorods having CTAB and mPEG (80 pM) in complete media having 10% DCS for 24 h. Most intense band was recognized as the serum albumin protein in the supernatant separated from different aspect ratios of Au nanorods. Complete media having 10% DCS and DCS free media was used as control experiments.

2.3.2 Cell Viability Studies with Gold Nanorods

Cytotoxicity studies of CTAB functionalized Au nanorods were carried out with HeLa cells at time intervals of 3, 6, 10, and 24 h (Figure 2.5C). Approximately 100% of the cells were viable for all aspect ratios of Au nanorods after incubating for 3 h. For Au nanorods of aspect ratios 2.6 and 5.4, the cell viability quickly dropped below 5% over a 24 h period. About 50-60% of the cells survived after incubating with Au nanorods of aspect ratio 3.2 and 11.5 for 24 h (Figure 2.5B). Importantly, these results indicate that there was no direct correlation between the aspect ratio of the nanorods and cell viability. Cytotoxicity studies with mPEG stabilized Au nanorods show that 80% of the cells survive under the same nanorod concentrations and incubation times (Figure 2.5B). These data are consistent with the non-toxic nature of mPEG-functionalized Au nanorods as reported in the literature.[48,69]

CTAB functionalized nanoparticles have been shown to be toxic for various cell lines including HeLa cells, bronchial epithelial cells and adult stem cells.[17] However, there are some discrepancies in the literature as to whether CTAB facilitates cell endocytosis, whether or not this stabilizer is toxic in general, or only toxic to specific cell types. The concentration of CTAB determines the size and shape of the Au nanorods during synthesis, but it is difficult to eliminate all traces of the toxic surfactant using washing steps and centrifugation prior to exposing the Au nanorods to cells.[8,9] Additionally, excessive washing (> 2×) causes the Au nanorods to form aggregates due to loss of CTAB on the surface. In this study, a strong correlation was observed between cell viability and free CTAB present in the media, but not with the aspect ratio of the Au nanorods. Figure 2.5A shows that the viability of HeLa cells is reduced upon exposure to the supernatant resulting from the washing steps (2×) of the Au nanorods. The supernatant can contain CTAB, $AgNO_3$, and hydroquinone depending on the protocol used for the synthesis of Au nanorods. The concentration of CTAB used for the synthesis of nanorods of AR 2.6 and 5.4 was 0.2 M and for ARs 3.2 and 11.5 was 0.1 M. The results in Figure 2.5A suggest that there is more

unbound (free) CTAB in the supernatant when higher concentrations of CTAB are used in the synthesis of Au nanorods, and that free CTAB is the main cause of cell death.

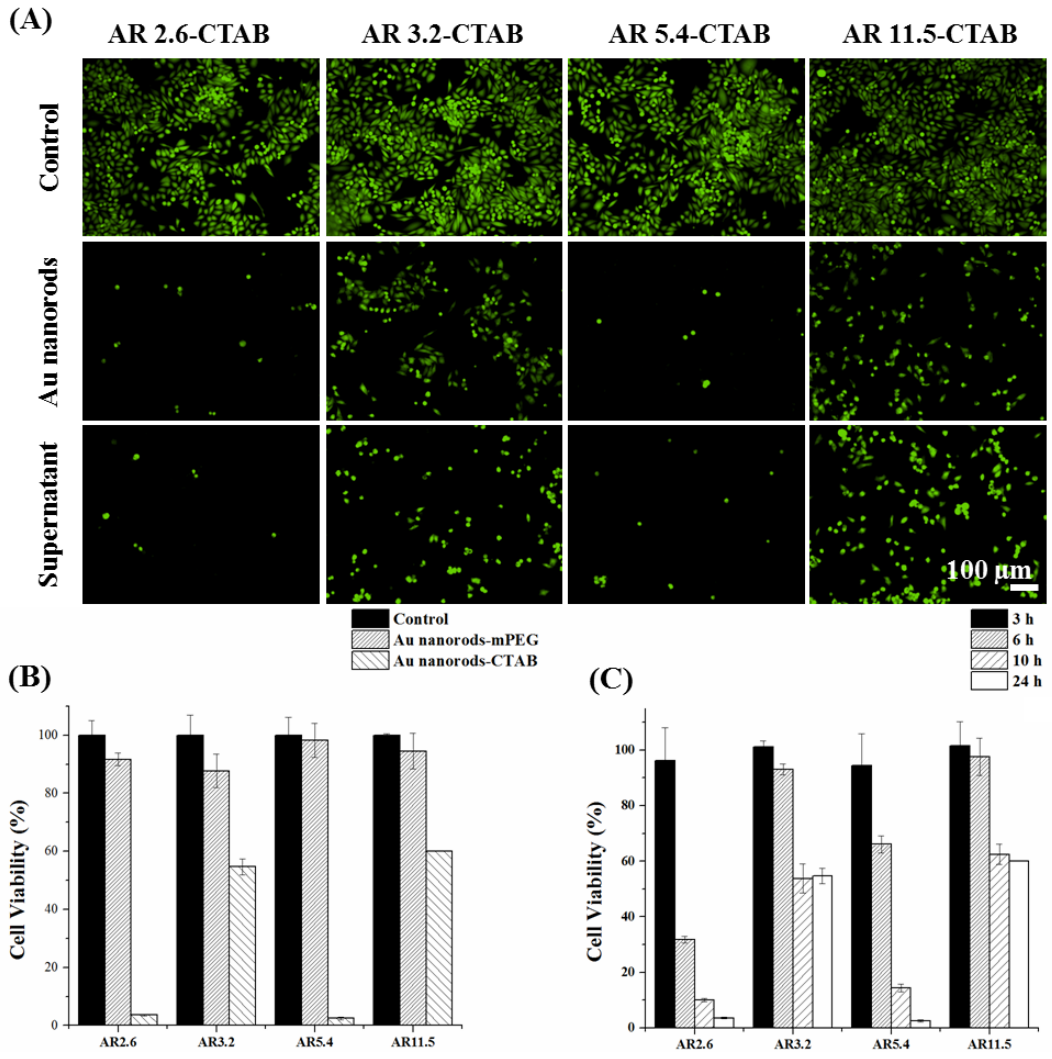

Figure 2.5. Fluorescence microscopy images of live/dead assay with live HeLa cells stained with Calcein Am green fluorescence dye. A) Images of viable cells after incubating (24 h) with complete media (control: cells not exposed to Au nanorods or supernatant), CTAB functionalized Au nanorods (80 pM) of different aspect ratios (2.6, 3.2, 5.4 & 11.5), and nanorod supernatant. B) Comparison between the cell viability of HeLa cells after 24 h treatment with CTAB and mPEG functionalized Au nanorods of four different aspect ratios. C) Graph of the cell viability of HeLa cells upon exposure to different aspect ratios of Au nanorods (80 pM) stabilized with CTAB as a function of time. Standard deviations were calculated from triplicate experiments.

Figure 2.6A shows a control experiment with HeLa cells exposed to various concentrations of free CTAB. There is nearly a 65% reduction in the viability of HeLa cells at a concentration of 20 μM over a 24 h period. The concentration of free CTAB in our experiments was estimated to be between 20 μM to 60 μM when considering the dilutions during the washing steps of the Au nanorods. The significant drop in cell viability upon exposure to free CTAB correlates well with the significant cell death upon exposure to supernatant alone as illustrated in Figure 2.5A. To show that CTAB and not another supernatant component was responsible for reduced cell viability, the effect of $AgNO_3$ on cell viability was also evaluated for comparison. Au nanorods of ARs 2.6, 3.2 and 5.4 were synthesized with $AgNO_3$ concentrations of 100 μM, 60 μM and 350 μM, respectively. No $AgNO_3$ was added during the synthesis of Au nanorods of AR 11.5. Figure 2.6B shows the effect of standard solutions of $AgNO_3$ on cell viability. Exposure to a 1 μM solution of $AgNO_3$ resulted in a 20% reduction in cell viability. The concentration of unreacted Ag^+ was estimated to be between 0.5 μM to 10 μM considering that $AgNO_3$ was diluted in the washing steps during the isolation of the Au nanorods. Murphy and co-workers have shown that a Ag^+ concentration of less than 5 μM is non-toxic to the HeLa cells,[65] suggesting that these lower levels of Ag^+ used here would not be detrimental to HeLa cells. Protocols for the synthesis of nanorods of AR 2.6 and 5.4 utilized both a higher concentration of CTAB (0.2 M) and $AgNO_3$. It cannot be completely ruled out that there may be an additive effect on viability when cells were exposed to both higher concentrations of CTAB and $AgNO_3$. However, the magnitude of cell death is not consistent with $AgNO_3$ being the primary cause of cell death in these experiments (Figure 2.6B). Nanorods of AR 3.2 and 11.5, however, used the same concentration of CTAB (0.1 M) and showed similar cell viabilities even though the synthetic process of Au nanorods with an AR of 11.5 was free of Ag^+. This data strongly suggests that free (unbound) CTAB has a significantly higher effect on cell viability than $AgNO_3$. For Au nanorods of AR 11.5, a slightly higher viability was observed than AR 3.2. This may be due to the initial purification process that utilized sedimentation and, which may have resulted in a slightly lower amount of CTAB in the

supernatant than if centrifugation was used to isolate of the nanorods instead. Since the synthesis of AR 5.4 used hydroquinone as the reducing agent, the toxicity of free hydroquinone was also analyzed. Hydroquinone is toxic at a concentration as low as 0.5 µg/mL. The concentration of hydroquinone in the supernatant of AR 5.4 was determined to be ~0.02 µg/mL by UV-Vis spectrometry. The cell viability in this system is quite similar to AR 2.6, a system that used $NaBH_4$ as the reducing agent (Figure 2.5B). Based on this data, it does not appear that hydroquinone has an evident effect on cell viability (at this concentration). Taken together, the data show that there is a strong correlation between free CTAB and cytotoxicity. This work is consistent with the work of Murphy and others.[14,65,17,70] The goal of these experiments was to determine whether a correlation between the aspect ratio of the Au nanorods and cytotoxicity exists, but no such conclusion could be reached given that free CTAB has an inordinate effect on cytotoxicity.

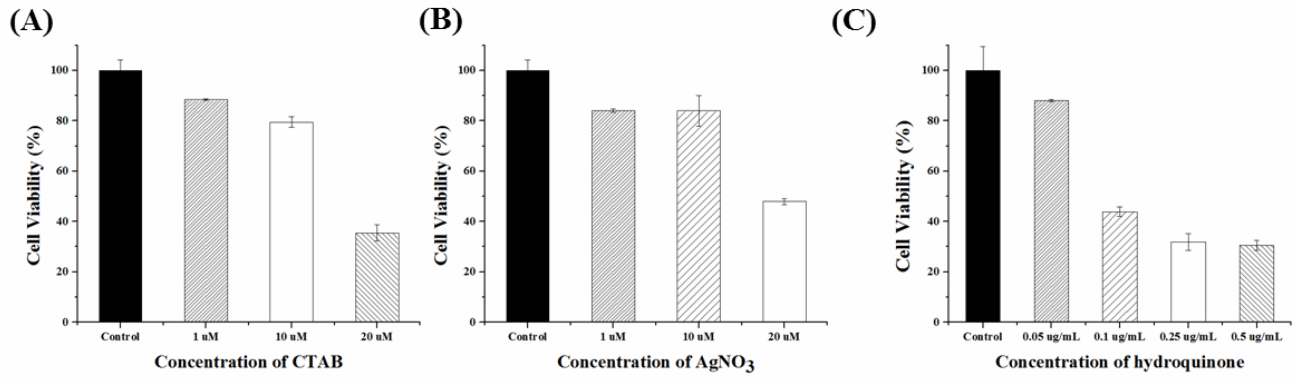

Figure 2.6. Cell viability studies of HeLa cell after incubating for 24 h as a function of A) different concentrations of CTAB (1 µM, 10 µM and 20 µM); B) concentrations of $AgNO_3$ (1 µM, 10 µM and 20 µM); and C) concentrations of hydroquinone (0.05 µg/mL, 0.1 µg/mL and 0.25 µg/mL, 0.5 µg/mL). Standard deviations resulted from triplicate experiments are denoted by error bars.

2.3.3 Cellular Uptake of Gold Nanorods

ICP-AES measurements were conducted to estimate the amount of Au internalized by HeLa cells. After a 3-24 h incubation period with a Au nanorod concentration of 80 pM, cells were digested in aqua regia and the concentration of Au^{3+} was measured in a matrix of 3% HCl by ICP-AES (see Experimental Section). Using the concentration of Au^{3+} from ICP-AES experiment, the number of Au nanorod internalized per cell was calculated by estimating the amount of Au in an average sized Au nanorod. Figure 2.7A shows a plot of the concentration of Au per cell versus time for all four aspect ratios of Au nanorods. The most striking result is that a significantly higher cell uptake ($p < 0.001$) was observed for CTAB-stabilized Au nanorods of AR 11.5 at all-time points. Both the viability and the internalization (Figure 2.7A) of the Au nanorods were much higher for AR 11.5 than all other aspect ratios including nanorods functionalized with mPEG (Figures 2.8A & B). A slightly higher uptake was observed for CTAB functionalized nanorods of AR 3.2 compared to AR 2.6 ($p < 0.05$) and 5.4. This data is consistent with the cell viability study (Figure 2.5C). Cells exposed to nanorods that were synthesized with a higher CTAB concentration (0.2 M) resulted in higher cell death and, thus, the sample consisted mostly of live, adherent cells being analyzed by ICP-AES. [Note that analyzing dead cells would complicate the study since nanorods in the media could not be easily differentiated from those that were internalized and released upon apoptosis.] HeLa cells internalized a significant number of CTAB functionalized Au nanorods of AR 3.2 after a 24 h period. [Note: Longer time points were not considered here, however, since media exchanges would affect the overall nanorod concentration.] Since lower aspect ratio nanorods (AR 3.2) remain dispersed in the media for a longer time than the larger aspect ratio nanorods (11.5), it is likely that the difference in uptake may not necessarily be related to a size-dependent endocytosis mechanism but to the time point at which the nanorods physically come in contact with the cells. Åbergand[71] and Xia[72] have also shown that physical contact may be necessary for endocytosis of Au nanorods.

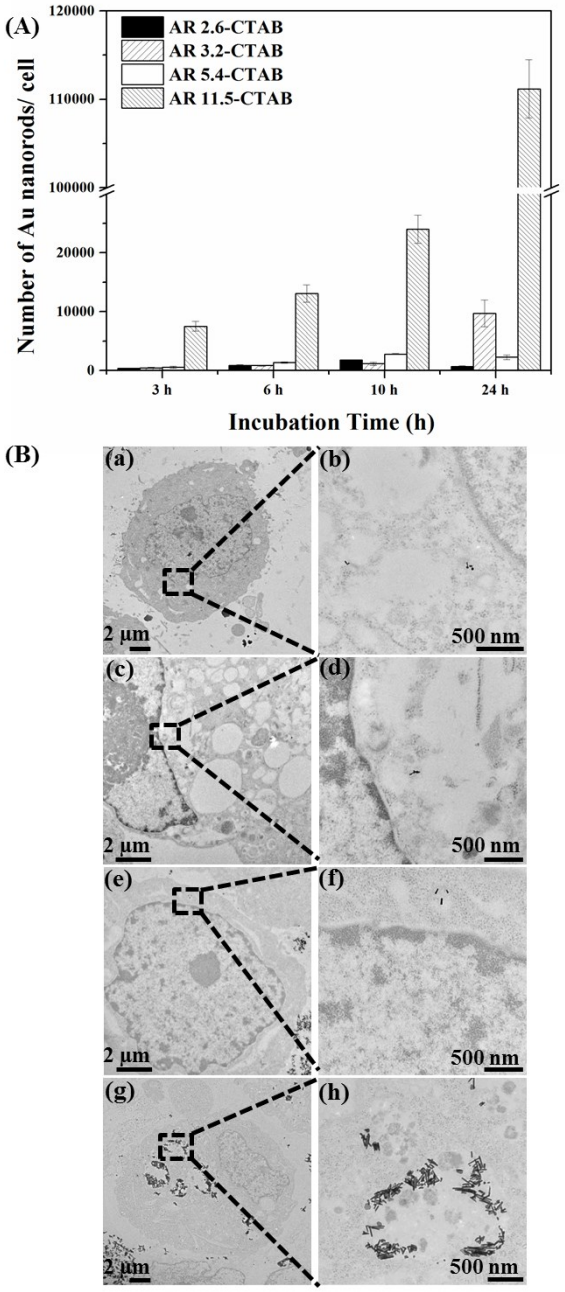

Figure 2.7. A) Cellular uptake studies conducted by using ICP-AES after incubating HeLa cell for 3 h, 6 h,10 h and 24 h with different aspect ratios of Au nanorods (80 pM) having CTAB. Experiments were performed in triplicates. B) TEM images of HeLa cells treated with CTAB functionalized Au nanorods (80 pM) for 24 h; (a,b) AR 2.6, (c,d) AR 3.2 (e,f) AR 5.4 (g, h) AR 11.5-CTAB.

Investigators have shown that albumin proteins adsorb on the surface of the CTAB-functionalized nanorods, forming a protein corona that results in higher rates of endocytosis in HeLa cells.[70] Given the changes in zeta potential of CTAB functionalized nanorods upon exposure to media (Figure 2.3), it is clear that a protein adsorption occurs in this case too. Taken together, the results of our experiments show that the aspect ratio of Au nanorods does not alone affect the endocytosis of nanorods, but also the other chemical components or impurities from the synthesis, such as CTAB, will also affect the cellular interactions and overall internalization.

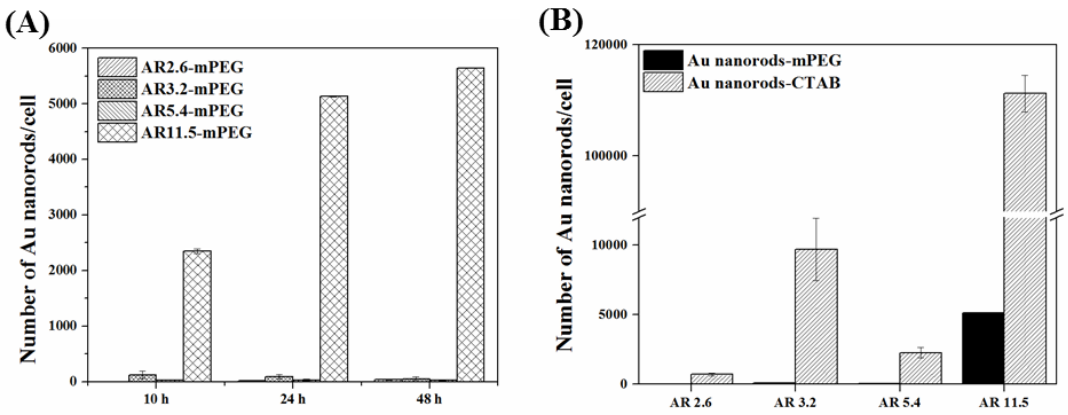

Figure 2.8. A) Cellular uptake studies conducted using ICP-AES after incubating HeLa cell for 10 h, 24 h and 48 h with different aspect ratios of mPEG functionalized Au nanorods (80 pM). B) Comparison of cellular uptake of CTAB & mPEG functionalized different aspect ratios of Au nanorods (80 pM) using ICP-AES after incubating with HeLa cell for 24 h. Experiments were performed in triplicates.

2.3.4 TEM Studies

Experiments were reproduced at a larger scale (6×) in order to generate enough cells for embedding and sectioning for TEM studies (see Experimental Section). Figure 2.7B shows TEM images of HeLa cells upon exposure to Au nanorods for 24 h. Consistent with the ICP-AES data, TEM experiments show that the largest AR of CTAB functionalized Au nanorods had the highest cellular uptake. These larger nanorods were localized primarily in the endosomes as clusters rather than individual particles (Figure 2.7). A few short rods, discoid and triangular shaped

particles were also observed inside the endosomes since the synthesis protocol for Au nanorods of AR 11.5 can yield a broad range of other shapes. Using sedimentation to isolate the particles and size-selective centrifugation for purification yields mostly nanorods (82% of long rods and 18% of small rods). Small amounts of low AR Au nanorods that were visible inside the cells were predominately in the cytoplasm (Figure 2.7B(a) to B(f)). The Au nanorods at an AR of 11.5 are currently the highest aspect ratio nanorods to be internalized by mammalian cells. This represents an experimental verification of a theoretical study by Zhang and co-workers[73] that predicted higher uptake for spherocylindrical particles with higher aspect ratios due to an increase in the bending energy which is required for the higher uptake of nanoparticles with the increase of the aspect ratio. Additionally, the quantity of internalized mPEG stabilized Au nanorods by HeLa cells was quite low (Figure 2.9). TEM images of HeLa cells show low endocytosis of Au nanorods, which is consistent with ICP-AES data. The low uptake is probably due to the poor interaction between mPEG molecules and the cell membrane.[61,67] Short mPEG functionalized nanorods were found as clusters in the cytoplasm (Figure 2.9).

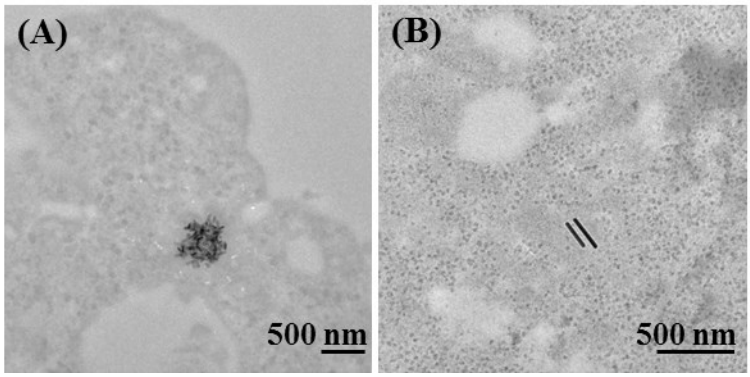

Figure 2.9. Magnified TEM images of HeLa cells treated with mPEG functionalized Au nanorods (80 pM) for 24 h. A) AR 5.4-mPEG and B) AR 11.5-mPEG.

2.4 CONCLUSION

This study demonstrated that the cell viability does not depend on the aspect ratio of Au nanorods alone and that the supernatant composition has a significant effect on cell viability. Au nanorods with aspect ratio 11.5 showed higher internalization compared to shorter aspect ratios. It is clear that the differences in the synthesis protocols, functionalization, and purification process also have a major effect on cellular uptake and not just the aspect ratio alone. Contrary to other experimental studies, the higher AR nanorods were readily internalized and at a higher cell viability when the stabilizer (CTAB) is surface bound. It is expected that cells treated with AR 11.5 nanorods may be useful for cellular imaging and laser photo-thermal therapy.

CHAPTER III

SYNTHESIS OF THE MATASTABLE PHASE OF GOLD PHOSPHIDE

Note: This chapter was published in *J. Solid State Chem.*, **2016**, *242*, 182-192. DOI: 10.1016/j.jssc.2016.07.009, and reprinted with permission.

3.1 INTRODUCTION

Transition metal phosphides have shown unique physical properties which makes them useful in the semiconductor industry,[74] and as electronic devices[75] and magnetic devices.[76] Most importantly, nanoscale transition metal phosphides have been widely studied as catalysts in the hydrogen evolution[77-83] and hydrodesulfurization[77,84-98] reactions that have led to greater interest in synthesizing these materials at the nanoscale. As a result, several synthetic protocols such as high temperature annealing of organometallic or solid-state precursors,[99,100] reactions of organometallics,[101] solvothermal reactions,[102] reactions of metal nanoparticles with phosphine or other phosphorous precursors[103,104] and thermal decomposition reactions of single-source precursors[105-107] have been developed to synthesize nanostructured transition metal phosphides. Thermal decomposition of tri-*n*-octylphosphine (TOP) is the most widely used method used to produce a variety of transition metal phosphides including Ni_2P, Ni_5P_4, PtP_2, Rh_2P, Cu_3P, FeP, and MnP, among others.[76,103,104,108,110]

In 1991 year, Weizer and Fatemi[111] carefully studied the interface of the Au-InP system, where the metallized gold was used to make electrical contacts with the InP semiconductor, they reported the formation of Au_2P_3 at the interface which resulted in a drop in contact resistivity by two-to-three orders of magnitude depending on the thickness of the Au_2P_3 at the metal–semiconductor interface. This work demonstrated that the Au_2P_3 has unique electronic properties that can be useful in the semiconductor industry. Although there is a great interest in developing the synthesis protocols to study the properties of metal phosphides, only a few studies have reported on the synthesis of gold phosphide (Au_2P_3).[103,112,113] Many physical properties of Au_2P_3 have not been sufficiently studied at the nanoscale since it is a challenging material to synthesize in bulk and no methods are currently available to control the purity, shape, or size of Au_2P_3 nanoparticles. For the synthesis of Au_2P_3, solution synthesis methods result in large amounts of gold impurities and the resulting morphology is difficult to control at the nanoscale. The goal of this work is to explore solution-synthesis methods to generate Au_2P_3 by examining the reactivity of ligand stabilized gold nanorods towards phosphorous incorporation.

Here, we focus on a synthesis method developed by Henkes et al.,[103,104] where metal nanoparticle templates are used to retain the shape of the resulting transition metal phosphide. [114-116] We illustrate that the surface capping agents on the precursor gold nanoparticle templates can affect the purity and extent to which the metastable gold phosphide phase will form using either 1-dodecanethiol or cetyltrimethylammonium bromide (CTAB) as surface capping agents. We demonstrate that thiol- functionalized gold nanorods undergo digestive ripening to produce uniform spherical particles under the reaction conditions required to decompose tri-*n*-octylphosphine (TOP) into elemental phosphorous. The thiol-functionalized gold nanoparticles showed reduced reactivity towards phosphorous incorporation and resulted in lower conversion of the gold nanoparticles to gold phosphide. In contrast, phase pure Au_2P_3 can be obtained when CTAB functionalized gold nanorods are used as the metal precursor. Interestingly, Au_2P_3 was

found to phase separate during TEM imaging experiments. The synthesized Au_2P_3 nanoparticles were evaluated for catalytic activity towards the hydrogen evolution reaction (HER). We find that the gold phosphide particles exhibit higher activity than polycrystalline gold.

3.2 EXPERIMENTAL SECTION

3.2.1 Chemicals

Tri-*n*-octylphosphine (TOP, 90%) and tri-*n*-octylphosphine oxide (TOPO, 98%) were purchased from Alfa Aesar. Hexadecyltrimethylammonium bromide (CTAB, >99%), Gold (III) chloride trihydrate (99.999%), sodium borohydride (99.99%), L-ascorbic acid (>98%), silver nitrate (>99%), and l-dodecanethiol (DDT, >98%) were purchased from Sigma-Aldrich. All chemicals were used without further purification, and all solutions, except gold (III) chloride trihydrate and CTAB were prepared freshly using deionized water (18.2 MΩ). Dedicated glassware was cleaned with before each reaction with aqua regia and then rinsed with deionized water. Handling of TOP was carried out in a dry, nitrogen atmosphere by using standard Schlenk line and glove box techniques.

3.2.2 Synthesis of Gold Nanorods

Au nanorods were synthesized by the seed mediated method as described elsewhere[43] with minor modifications. The seed solution consisted of CTAB (0.2 M, 5.00 mL), $HAuCl_4 \cdot 3H_2O$ (0.5 mM, 5.00 mL), and $NaBH_4$ (0.01 M, 600 μL). After stirring vigorously for 2 min., the solution was stored at 27 ˚C, and used immediately after aging (2 h-3 h). The growth solution consisted of CTAB (0.2 M, 5.00 mL), $HAuCl_4 \cdot 3H_2O$ (1 mM, 5.00 mL), and $AgNO_3$ (4 mM, 250 μL). Ascorbic acid (78.8 mM, 70 μL) was pipetted into the growth solution and swirled until it became colorless. Next, the seed solution (12 μL) was added to the growth solution and kept overnight at 27 ˚C. The nanorods were isolated *via* centrifugation (8000 rpm, 30 min.) and

washed twice in deionized H_2O. Au nanorod quality was verified by UV-Vis spectrophotometry. Once dried, Au nanorods functionalized with CTAB were dispersed in TOP by sonication and stored in a vacuum desiccator in preparation for the phosphide reaction.

3.2.3 Ligand Exchange

Gold nanorods functionalized with CTAB were dispersed in a mixture of nanopure H_2O (1.00 mL), acetone (2.00 mL), and 1-dodecanethiol (1.00 mL) in a 5 mL-glass vial. The suspension was sonicated (5 min.), vortexed (5 min.) and allowed to phase separate. After 1 h, Au nanorods were separated into the organic phase and isolated *via* centrifugation (8000 rpm, 30 min.). The Au nanorods were washed with ethanol to remove excess thiol and dispersed in TOP by sonication in preparation for the phosphide reaction.

3.2.4 Synthesis of Au_2P_3

The Au_2P_3 conversion reaction protocols were adopted from Henkes et. al.,[103,104] with minor modifications. In a typical reaction, TOPO (2.53 g) was heated to 120 ˚C for 1 h under an inert atmosphere while stirring with a glass stir bar. After raising the temperature to 360 ˚C, Au nanorods (3.9 mg) dispersed in TOP (5.1 mL) were injected into the hot TOPO. The reaction time was varied from 1-10 h. A ratio of 1:1 or 2:1 of TOP/TOPO was used as the phosphorous/solvent source. During the course of the 10 h reaction, the color of the solution transformed from purple to green and finally to dark brown, indicating the formation of Au_2P_3. The reaction was allowed to cool to 100 ˚C and saturated with ethanol. The black product was recovered by centrifugation using chloroform to remove unreacted TOP and TOPO.[98] Nanoparticles were dispersed in ethanol and kept in a vacuum desiccator prior to characterization to limit oxidation of the TOP coating on the surface of the particles.

3.2.5 Characterization

Nanoparticles were characterized using JEOL-JEM transmission electron microscope (TEM) operating at an accelerating voltage of 200 kV. Samples for TEM analysis were prepared by drying a 2 μL of ethanol containing nanoparticles on carbon coated copper grid. X-ray powder diffraction data were collected using a Rigaku SmartLab X-ray diffractometer (Cu Kα radiation). The UV-Visible analysis was carried out using DU 530 Beckman Coulter UV-Visible spectrophotometer. IR spectra were collected on a Nicolet iS50 ATR-FTIR spectrometer.

3.2.6 Hydrogen Evolution Reaction Experiments

An Autolab single channel potentiostat from Eco Chemie, Metrohm Autolab B.V. was used to obtain electrochemical measurements. For the purpose of controlling the rotation of the working electrode, modulated speed rotator (Pine Instrument Company) was used. A homemade reversible hydrogen electrode (RHE) was used as the reference electrode having glass tube containing hydrogen-saturated $HClO_4$ acid (0.1 M) and a Pt wire connected to the main electrochemical cell by a Luggin capillary. The working electrode was prepared by coating Au_2P_3 nanoparticles onto glassy carbon (5 mm diameter, area 0.196 cm^2) at a loading of 50 $\mu g/cm^2$. Inks were prepared having 9.8 mg catalyst per 10 mL of ink (76% water, 24% 2-propanol). To improve the ink dispersion, Nafion ionomer (5 wt. %, Sigma Aldrich) was added at 40 μL per 10 mL of ink. Inks were sonicated in ice by horn sonication for 30 s, bath sonication for 20 min., and horn sonication again for 30 s. Onto each electrode 10 μL of ink were pipetted and air dried at 40 °C for 20 min. Since the electrodes were not active for HER, electrochemical break-in (50 cycles, -0.3 to 1.6 V) was used in 0.1 M $HClO_4$ acid and HER/HOR (hydrogen oxidation reaction) activities were taken anodically (scan direction did not appear to matter). Rotating disk electrode (RDE) was used to measure the activities using reversible hydrogen electrode (RHE) as the

reference while having Au mesh counter electrode and activities were also corrected for internal resistance.

3.3. RESULTS AND DISSCUSION

Different from previous studies, the gold nanoparticle morphology was controlled in order to determine effect of the morphology of the gold nanoparticle reactants on the resulting morphology of the gold phosphide product. Since the work done by Sanchez[113] showed the formation of 1D structures of Au_2P_3 when synthesized in solution, we chose to study gold nanorods as a morphological template to promote the formation of rod shaped Au_2P_3 particles in the final product and also to determine whether the morphology of the gold nanoparticle reactants affected the resulting morphology of the gold phosphide. From the results obtained, it is clear that the gold nanorod templates undergo dissolution in the process of generating Au_2P_3 and do not significantly affect the final Au_2P_3 morphology. The gold nanorods simply act as a reagent rather than a template. The purity of Au_2P_3 was affected by the capping agent on the surface of the gold nanorods, either 1-dodecanethiol or CTAB. With the use of 1-dodecanethiol as surface capping ligand on the precursor Au nanorods, spherical nanoparticles of Au_2P_3 were produced showing less likelihood to agglomerate and sinter. The use of CTAB, a weaker surface stabilizer produced Au_2P_3 in a higher purity and yield.

3.3.1 Characterization of Gold Nanorods

Gold nanorods were synthesized using a seed mediated method with CTAB as the stabilizing agent.[53] Gold nanorods showed characteristic surface plasmon resonance (SPR) bands in the UV-Visible spectrum (Figure 3.1B) having the mean dimensions of 57 nm × 24 nm (length × width) as seen in TEM images (Figure 3.1A). Surface plasmon resonance bands, which correspond to the transverse and longitudinal oscillation modes of the gold nanorods, appear at 520 nm and 660 nm, respectively.

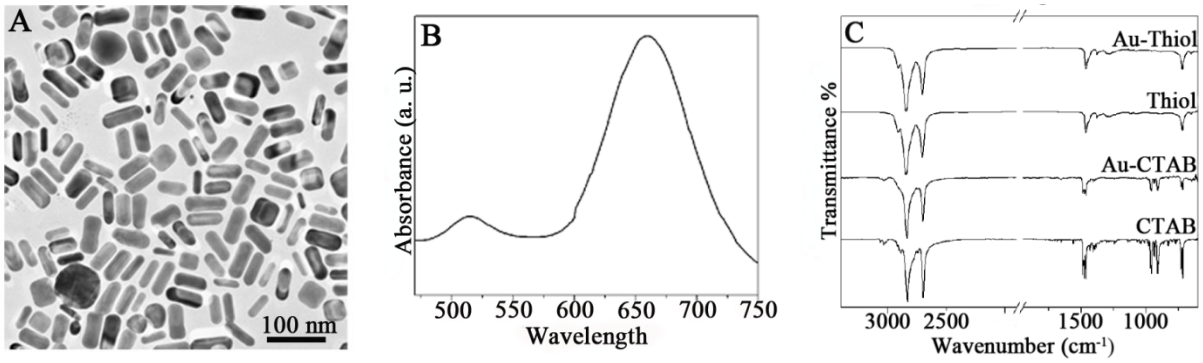

Figure 3.1. Characterization of surface functionalized gold nanorods. A) TEM image of gold nanorods synthesized using the seed-mediated method with CTAB as the surface stabilizer. B) UV-Vis absorption spectra of CTAB functionalized gold nanorods with SPR bands at 520 nm and 660 nm. C) ATR-FTIR spectra of the gold nanorods prior to and after ligand exchange with 1-dodecanethiol. From top to bottom: gold nanorods after ligand exchange with 1-dodecanethiol (Au-Thiol), neat 1-dodecanethiol (Thiol), gold nanorods functionalized with CTAB (Au-CTAB), and neat CTAB.

For the purpose of studying the effect of surface capping agents on gold phosphide conversion reactions, the CTAB bilayer on the gold nanorods was replaced with 1-dodecanethiol as mentioned in the Experimental Section. Figure 3.1C represents the ATR-FTIR spectra of the gold nanorods before and after the functionalization with 1-dodecanethiol. Characteristic peaks at 3014 cm^{-1} and 1040 cm^{-1} correspond to the asymmetric $N(CH_3)_3^+$ and C-N stretching vibrational modes of CTAB while bands at 2900 cm^{-1} and 1460 cm^{-1} are characteristic to the CH_3 and CH_2 stretching vibrations. After functionalizing with 1-dodecanethiol, gold nanorods show three distinct bands at 2954 cm^{-1}, 2921 cm^{-1} and 2852 cm^{-1}, together with the weak peak around 1280 cm^{-1} that can be assigned to CH_3 asymmetric stretching, CH_2 asymmetric stretching, CH_2 symmetric stretching and CH_2-S wagging vibration, respectively. Peaks for CH_2 rocking and C-S stretching of 1-dodecanethiol also appeared at 720 cm^{-1} and 654 cm^{-1} proving the presence of 1-

dodecanethiol on the Au nanorod surface. The absence of C-N and $N(CH_3)_3^+$ peaks that correspond to CTAB also indicate complete ligand exchange from CTAB to the thiol.

3.3.2 XRD Analysis

A coordinating solvent mixture of TOP/TOPO was reacted separately with CTAB and 1-dodecanethiol functionalized gold nanorods at 360 °C. TOP acts as the reactive species that produce phosphorous *in situ* by decomposition at elevated temperatures and TOPO act as the solvent for the reaction.[104] As shown in Figure 3.2, limited conversion to the Au_2P_3 was observed when 1-dodecanethiol functionalized gold nanorods were reacted in a 1:1 ratio of TOP/TOPO for 1 h to 10 h of reaction time. Powder XRD analysis of the resulting nanocrystalline products show gold as the major product, ($Fm\bar{3}m$, PDF card no. 00-001-1172). Major peaks at 2-Theta values of 38.2˚, 44.6˚, 64.7˚ and 77.5˚ correspond to the respective (111), (200), (220) and (311) planes of face centered cubic (FCC) gold. Between 1 h to 10 h of reaction times, small amounts of Au_2P_3 was formed as demonstrated by of minor peaks at 2-Theta = 32° that correspond to the (041) plane of the monoclinic phase (C2/m, PDF card no.01-071-0590) (Figure 3.2). The strong Au-S bond between the Au nanorods and 1-dodecanethiol limit the access to gold atoms at the surface while inhibiting the diffusion of phosphorous. Therefore, complete conversion to the Au_2P_3 phase was not possible with the use of 1:1 TOP/TOPO ratio with 1-dodecanethiol functionalized gold nanorods.

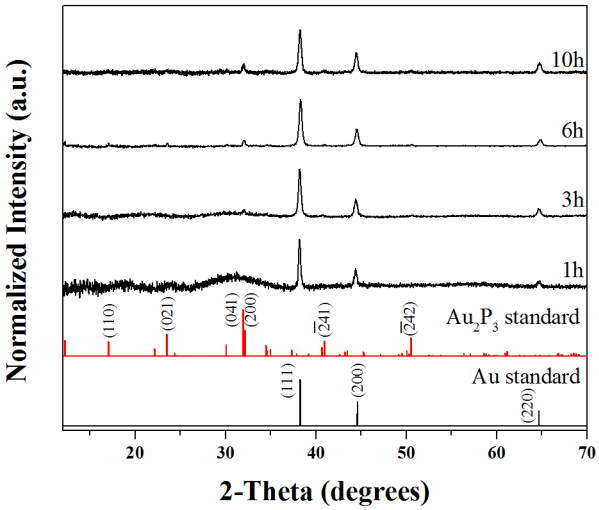

Figure 3.2. Powder X-ray diffraction patterns of nanocrystal products formed by reacting gold nanorods functionalized with 1-dodecanethiol with a 1:1 TOP/TOPO ratio for 1 h, 3 h, 6 h, and 10 h. All reactions were carried out at 360 °C. Gold nanoparticles were the major product. Peaks at 2 Theta = 32° demonstrate the formation of small amounts of Au_2P_3 from 1 h – 10 h.

When gold nanorods functionalized with 1-dodecanethiol were reacted with a 2:1 ratio of TOP/TOPO, higher yields Au_2P_3 particles were generated as shown in Figure 3.3. During the reaction, small quantities of Au_2P_3 were observed at 1 h and 3 h (Figure 3.3). XRD data show that the optimum reaction time was 6 h, where the monoclinic C2/m Au_2P_3 phase was the most prominent (Figure 3.3). The reactivity of the gold surface was still hindered by the thiol coating so complete conversion to the phosphide was not achieved. However, the higher concentration of TOP favors the formation of Au_2P_3 by increasing the partial pressure of the phosphorous generated *in situ*. Powder XRD analysis indicates that 6 h was the optimum reaction time and that decomposition of the Au_2P_3 monoclinic phase was observed at 10 h. This is most likely due to the vaporization and loss of phosphorous (Figure 3.3) because the reaction vessel is not completely closed to the environment and there is a possibility to observe fluctuations in the pressure of the system over the time. This could have resulted in the decomposition of the gold

phosphide phase or incomplete phosphorous incorporation especially at lower TOP concentrations, which may be one reason that gold phosphide is typically produced with large amounts of gold impurities.

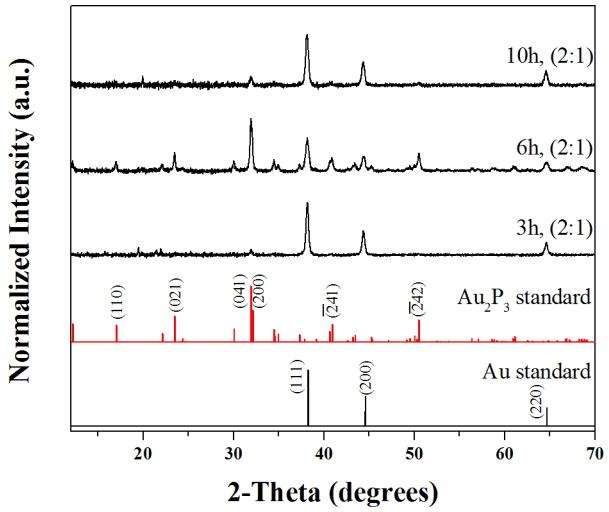

Figure 3.3. Powder X-ray diffraction patterns of nanocrystal products formed by reacting gold nanorods functionalized with 1-dodecanethiol with a 2:1 TOP/TOPO ratio for 3 h, 6 h, and 10 h. All reactions were carried out at 360 °C. Gold phosphide was the major product at 6 h but the phase decomposes by 10 h.

When CTAB was used as a capping agent instead of 1-dodecanethiol, a similar trend in the reactivity of the gold nanorods towards conversion to the gold phosphide was observed. Like the thiol reaction, when a 1:1 ratio of TOP/TOPO was used, only small quantities of the gold phosphide resulted at 1 h and 3 h (Figure 3.4). Compared to the thiol functionalized gold (Figure 3.2), larger quantities of Au_2P_3 were produced at 6 h when CTAB functionalized gold nanorods were reacted with 1:1 TOP/TOPO ratio. Au_2P_3 phase was the most prominent phase observed at 10 h of reaction time when CTAB was used as a surface stabilizer on the gold nanorod surface compared to the thiol. The increased reactivity of the gold nanorods is attributed to the weaker CTAB interactions between gold surfaces which make the gold surface more accessible for phosphorous incorporation. Since the conversion of gold to phosphide is more effective at 6 h

(Figure 3.4) with CTAB functionalized gold nanorods, the decomposition of the gold phosphide phase is not as evident at 10 h when compared to the reaction of thiol functionalized gold nanorods in a 1:1 TOP/TOPO ratio (Figure 3.2). With the use of 1:1 TOP/TOPO ratio and CTAB functionalized gold nanorods, both FCC gold and monoclinic Au_2P_3 (C2/m) crystalline phases were observed at 10 h as shown by powder XRD analysis in Figure 3.4.

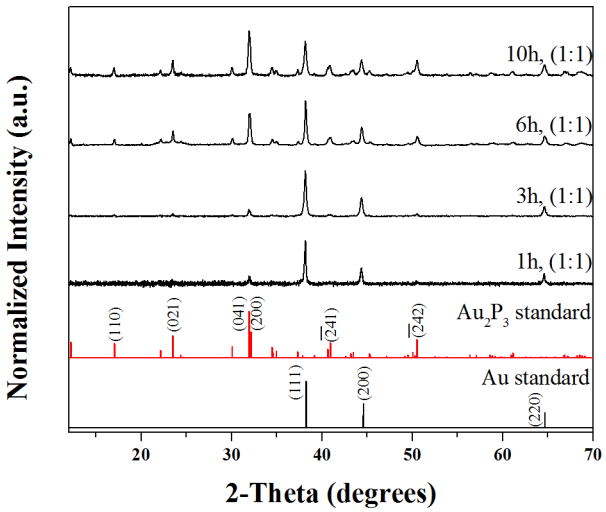

Figure 3.4. Powder X-ray diffraction patterns of nanocrystals formed after reacting gold nanorods functionalized with CTAB in a 1:1 TOP/TOPO ratio. Gold nanorods were converted to gold phosphide when reacted in a 1:1 TOP: TOPO ratio for 6 h at 360 °C. Gold impurities are present at 10 h.

For the purpose of improving the purity of the Au_2P_3 product, the TOP/TOPO ratio was further increased to 2:1 while maintaining CTAB as the gold surface stabilizer (Figure 3.5). As evident by the prominent reflections of Au_2P_3 in powder XRD analysis (Figure 3.5), increasing the reaction time to 6 h resulted in Au_2P_3 formation. Unlike the thiol system, it was possible to generate Au_2P_3 as the major phase at 10 h when reacting CTAB stabilized gold nanorods with a 2:1 TOP/TOPO ratio (Figure 3.5). Complete conversion of gold to gold phosphide is probably due to the synergistic effect of the weaker surface stabilizer and the higher amounts of TOP used during the reaction. A weaker surface stabilizer such as CTAB allows the surface to be more

reactive and the use of larger quantities of TOP affect the partial pressure of the gases produced in the reaction vessel which creates more favorable conditions for the synthesis of the Au_2P_3 phase (Figure 3.5). As shown in Figure 3.5, powder XRD analysis confirms the formation of the metastable monoclinic Au_2P_3 phase as the major product with the observation of peaks at 2-Theta values of 12.2˚ (020), 17.1˚ (110), 23.5˚ (021), 31.9˚ (041) and 32.1˚ (200) (PDF card no.01-071-0590). From these results, it is clear that both the surface stabilizer on the gold surface and the amount of TOP available for the reaction is important in obtaining Au_2P_3 in high yields.

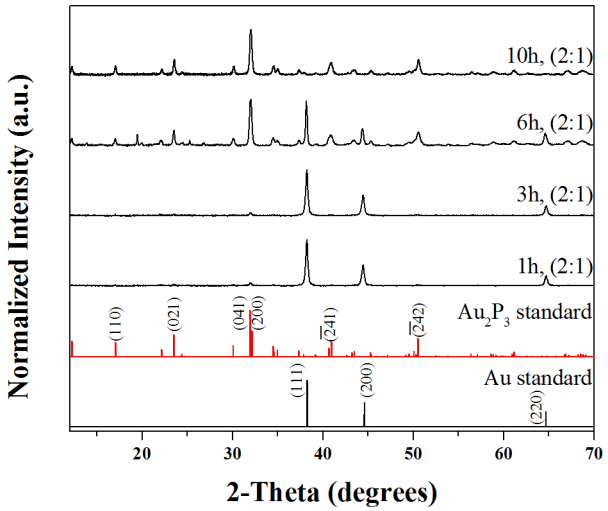

Figure 3.5. Powder X-ray diffraction patterns of nanocrystals formed after reacting gold nanorods functionalized with CTAB in a 2:1 TOP/TOPO ratio. Gold nanorods were converted to the gold phosphide phase after reacting for 6 h at 360 °C. Au_2P_3 is the major phase produced at 6 h and 10 h.

3.3.3 Characterization of Nanoparticle Products by TEM

To further confirm the results obtained in powder XRD, transmission electron microscopy (TEM) was used to characterize the nanoparticles resulting from the phosphide reactions. Little to no gold phosphide was observed by TEM when thiol functionalized gold

nanorods were reacted in a 1:1 TOP/TOPO ratio (Figure 3.6), as observed in powder XRD (Figure 3.2). In fact, gold nanoparticles were seen as the major product in this set of reactions.

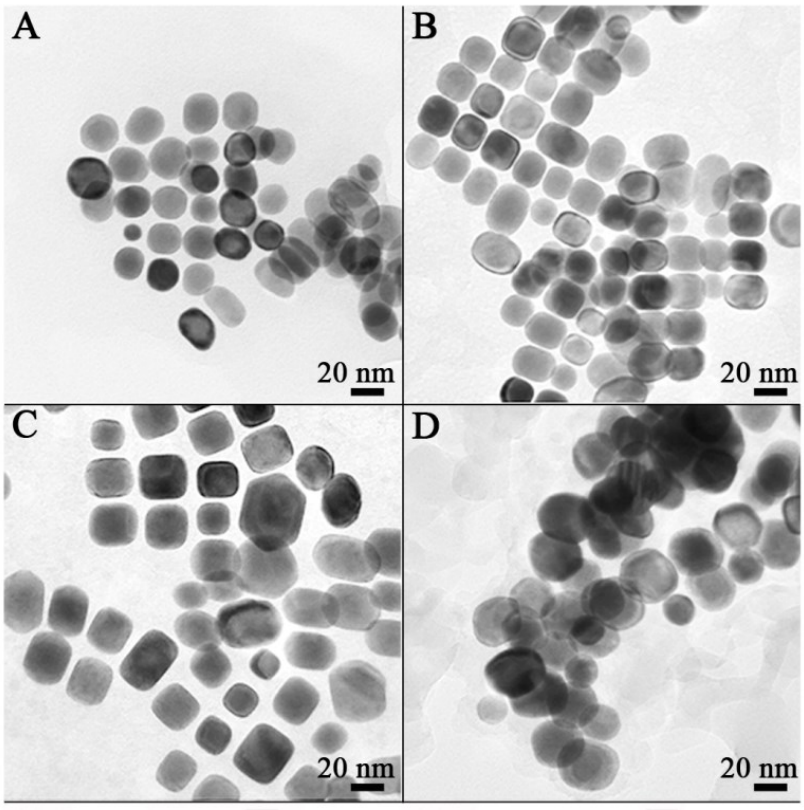

Figure 3.6. Time evolution of the morphology of gold nanorods functionalized with 1-dodecanethiol after reacting in a 1:1 TOP/TOPO ratio at 360 °C. TEM images of the gold nanoparticles after reacting for A) 1 h, B) 3 h, C) 6 h, and D) 10 h. The gold nanorods transform into cubes and rectangular shapes before yielding to spherical morphologies as they undergo digestive ripening through the course of the reaction.

As shown in Figure 3.6 TEM images highlight the change in morphology of the gold nanoparticles in these reactions. Figures 3.6A-D show images of the time evolution of the gold nanorod morphology after reacting with 1-dodecanethiol functionalized gold nanorods in a 1:1 TOP/TOPO from 1 – 10 h. Gold nanorods functionalized with thiol were changed into truncated rods and spherical particles with a mean size of 24 (±4) nm after reacting for 1 h (Figure 3.6A).

When the reaction was carried out for 3 h, small cubic gold nanoparticles were observed (Figure 3.6B). Later, these cubic particles formed truncated edges at 6 h (Figure 3.6C) and finally transformed into spheres when the reaction reached 10 h (Figure 3.6D). Lighter contrast regions observed by TEM images at the periphery of the cubic and spherical particles indicated the presence of core-shell structure as the reaction progressed (Figures 3.6C & D). However, the presence of phosphorous in the core-shell structures could not be verified by energy dispersive x-ray spectroscopy (EDX) due to the overlapping of phosphorous K-α peak and gold M peak. Although the lattice spacing of the lighter contrast regions corresponds to FCC gold (2.4 Å), this does not necessary disregard the formation of a core-shell structure (*e.g.* alloy formation at the shell). Further studies will be performed in the future to confirm the formation of a core-shell structure.

Studies done by Klabunde and others[117-119] have previously shown that the average size and the polydispersity of gold nanoparticles can be significantly reduced by refluxing the particles in the presence of alkylthiols. This process is known as digestive ripening where a colloidal suspension is heated to or near the boiling point of the solvent while having a surface-active ligand, which results in monodisperse spherical particles.[117-119] As shown in Figure 3.6, the change in the morphology and sizes of the gold nanorods is possibly due to a digestive ripening process that took place in the presence of 1-dodecanethiol and TOPO. According to the literature, monodisperse spherical particles of gold and other metals have been successfully synthesized through the digestive ripening process in the presence of TOPO and 1-dodecanethiol.[119] In the presence of TOPO and 1-dodecanethiol, rod shaped gold particles transformed into small cubes eventually leading to a spherical morphology with long reaction times and at a high temperature (Figure 3.6). This result contrasts to the work done by Henkes et al., where they used metal nanoparticles as a template to retaining the shape of the final phosphide products.[103]

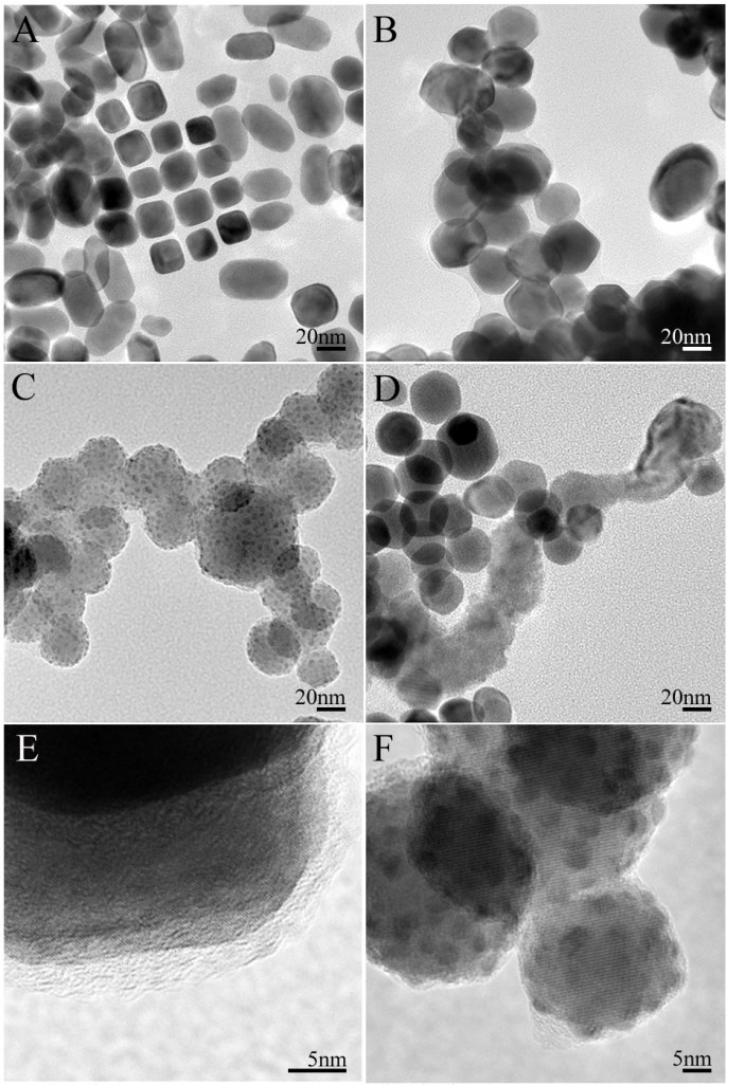

Figure 3.7. TEM images of the nanoparticles synthesized from the reaction of gold nanorods stabilized with1-dodecanethiol and TOP/TOPO in a 2:1 ratio. A) The morphology of the gold nanorods quickly evolves from rods to cubes after reacting with TOP/TOPO for 1 h. B) Gold particles with irregular shapes and rounded edges were the major product at 3 h. C) Nanospheres of Au_2P_3 decorated with gold nanoparticles (high contrast areas) were observed at 6 h. The unique morphology results from phase separation of gold to the surface of Au_2P_3. D) Decomposition of the Au_2P_3 phase was observed at 10 h, which results in gold particles as the major product. E) 3 h and F) 6 h confirm the particles to be gold (d_{111}= 2.3 Å) and gold phosphide (d_{110} = 5.1 Å), respectively.

Figure 3.7 shows the TEM images of nanoparticles produced by reacting gold nanorods functionalized with 1-dodecanethiol with a 2:1 ratio of TOP/TOPO. After a 1 h of the reaction,

gold nanorods were transformed into truncated rods and small cubic gold particles as shown in Figure 3.7A. At 3 h, gold nanoparticles were observed as the major product having a pseudo hexagonal or spherical morphology (Figure 3.7B). These changes in morphology are probably due to digestive ripening as mentioned previously. After the reaction utilizing 2:1 ratio of TOP/TOPO with thiol stabilized gold nanorods, spherical Au_2P_3 particles were produced at 6 h as shown in Figure 3.7C. Small gold particles of approximately 7 nm in diameter (high contrast dots) were observed on the surface of Au_2P_3. Little to no Au_2P_3 was observed by TEM analysis at 1 h and 3 h (Figure 3.7A & B). Larger quantities of Au_2P_3 were produced at 6 h (Figure 3.7C). At 10 h, decomposition of the Au_2P_3 phase was observed as shown in Figure 3.7D. High magnification TEM images of particles from a 3 h reaction and a 6 h reaction can be seen in Figures 3.7E and 3.7F and confirm that gold and Au_2P_3 were produced as evidenced by the lattice spacing of 2.3 Å and 5.1 Å that correspond to the Au (111) and Au_2P_3 (110) planes, respectively. It should also be noted that the observation of small gold nanoparticles on the surface of gold phosphide particles is due to phase separation (Figure 3.7F). When a 1:1 ratio of TOP/TOPO was used (Figure 3.6), low yields of gold phosphide was produced due to the strong binding of thiol ligand to the gold surface, which caused reduced reactivity on the surface. However, increasing the ratio of TOP/TOPO to 2:1 led to higher yields of gold phosphide even in the presence of a strong surface stabilizer such as 1-dodecanethiol. As observed in 6 h reaction, Au_2P_3 morphology remained spherical although the particles did undergo sintering (Figure 3.7F). This suggests the possibility of having size and shape control in the gold phosphide system with strong surface stabilizers. Although the thiol capping agents does limit the conversion efficiency of gold to gold phosphide, the vapor pressure appears to have a much larger effect. The vapor pressure of the gaseous phosphorous produced *in-situ* increased with the amount of TOP, and likely affected the yield and purity of the final product. As mentioned earlier, vaporization of phosphorous can result in the decomposition of gold phosphide back into its constituent elements during prolonged reaction times.

When gold nanorod precursors are functionalized with a weaker surface stabilizer such as CTAB, larger quantities of gold phosphide are generated in higher purities (Figure 3.8). As shown in Figure 3.8, after the CTAB functionalized gold nanorods are reacted with a 1:1 ratio of TOP/TOPO for 1 – 3 h (Figures 3.8A & 3.8B), spherical particles and large irregular shaped gold nanoparticles are generated. Since CTAB is a weaker surface stabilizer, the gold nanorods can quickly lose their morphology. Figures 3.8C and 3.8D show representative TEM images of the particles synthesized at 6 h and 10 h, respectively. The lighter contrast particles correspond to gold phosphide while the high contrast particles correspond to gold as confirmed by the high magnification TEM images of the resulting particles (Figure 3.9) (approximately 50% of the particles are gold phosphide). Interestingly, the gold phosphide particles are not very stable under the electron beam and phase separation occurs during TEM imaging experiments. Figure 3.8E tracks the decomposition of a gold phosphide particle synthesized from a 6 h reaction using a TEM imaging experiment. A rectangular box in Figure 3.8E TEM image highlights a Au_2P_3 particle at low magnification. Black arrows in the higher magnification later panels highlight the growth and fusing of gold particles on the surface of the same Au_2P_3 particle. The Au_2P_3 particles begin to decompose under the intense electron beam and segregate to the surface forming gold nanoparticles. With the formation of gold particles on the surface, the size of the gold phosphide particle decreases from 34 nm to 30 nm. However, throughout the imaging experiment, the interplanar spacing of 5.1 Å that corresponds to (110) plane of Au_2P_3 remained constant.

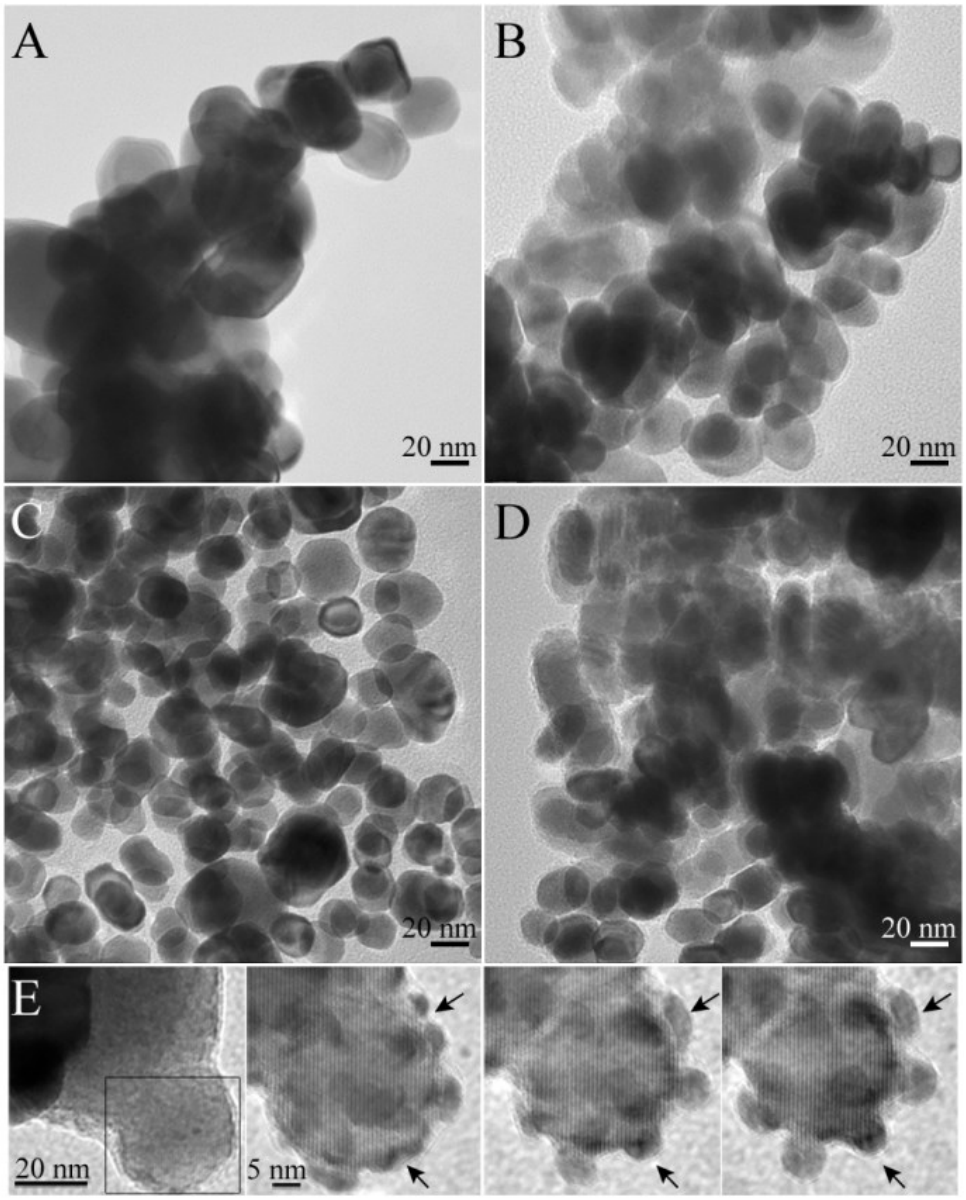

Figure 3.8. TEM images of the nanoparticles synthesized from the reaction of gold nanorods and TOP/TOPO in a 1:1 ratio. A) The morphology of the CTAB gold stabilized nanorods quickly changes from rods to irregular shaped particles after reacting with TOP/TOPO for 1 h. B) Gold particles with irregular shapes and rounded edges remain the major product at 3 h. A mixture of Au_2P_3 (low contrast particles) and gold (high contrast particles) were observed at C) 6 h and D) 10 h. E) Decomposition of a gold phosphide particle was followed by TEM imaging. The rectangular marquee highlights a Au_2P_3 particle. At low magnification, there are no gold particles on the surface of the phosphide particle. The arrows in the subsequent panels highlight the coalescence and growth of gold particles on the surface of the same Au_2P_3 particle at a higher magnification. Gold particles begin to segregate to the surface of Au_2P_3 particle under the intense electron beam. The interplanar spacing of 5.1 Å corresponds to (110) plane of Au_2P_3. [Note: The 5 nm scale bar corresponds to the last three panels taken at the same magnification.]

Within 1 minute of exposure to the electron beam of TEM, high contrast spots were observed due to the formation of gold particles. After 5 minutes of exposure to the TEM beam, the coalescence of the gold particles at the surface was quite prominent. Phase separation of gold to the surface of the gold phosphide nanoparticles was observed in several samples (Figures 3.7F & 3.8E). This could be due to the vaporization and loss of phosphorous during the TEM imaging experiments and/or diffusion of gold to the surface. Sanchez and co-workers also observed a similar composite structure where gold nanoparticles are embedded within a gold phosphide matrix (Au-Au_2P_3).[113] However, in their study, the formation of the composite was not described as an effect resulting from imaging experiments.

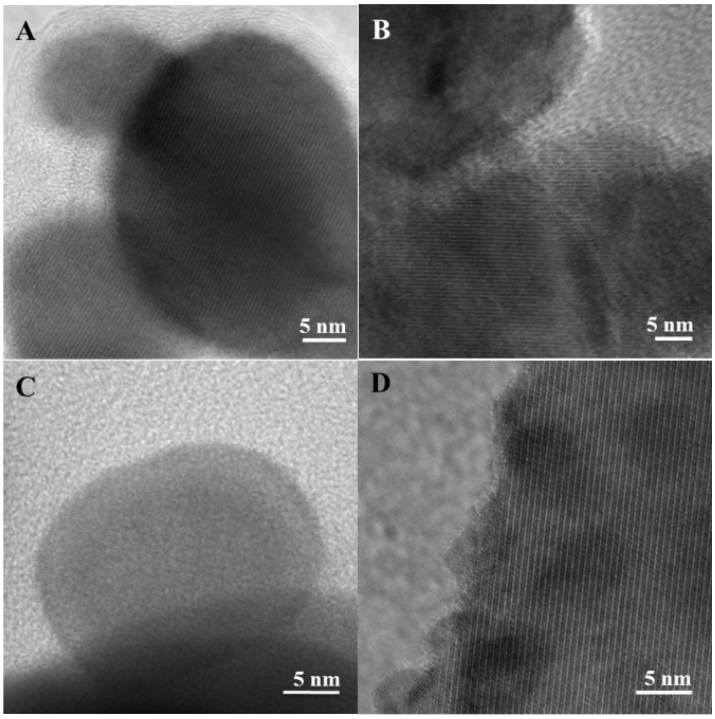

Figure 3.9. HRTEM images of Au_2P_3 formed by reacting CTAB stabilized gold nanorods with TOP/TOPO at 360 ˚C in a (A) 1:1 ratio for 3 h; (B) 1:1 ratio of 10 h; (C) 2:1 ratio for 3 h, and (D) 2:1 ratio for 10 h. Images (A), (B), and (D) show the interplanar spacing of 5.1 Å that correspond to the (110) planes of Au_2P_3 and image (C) shows the interplanar spacing of 2.7 Å that corresponds to the (041) plane of Au_2P_3.

By reacting CTAB functionalized gold nanorods with a TOP/TOPO ratio of 2:1, phase pure samples of Au_2P_3 could be prepared as shown in Figures 3.5 & 3.10. Figure 3.10 shows representative TEM images of the particles produced during the 1-10 h reaction.

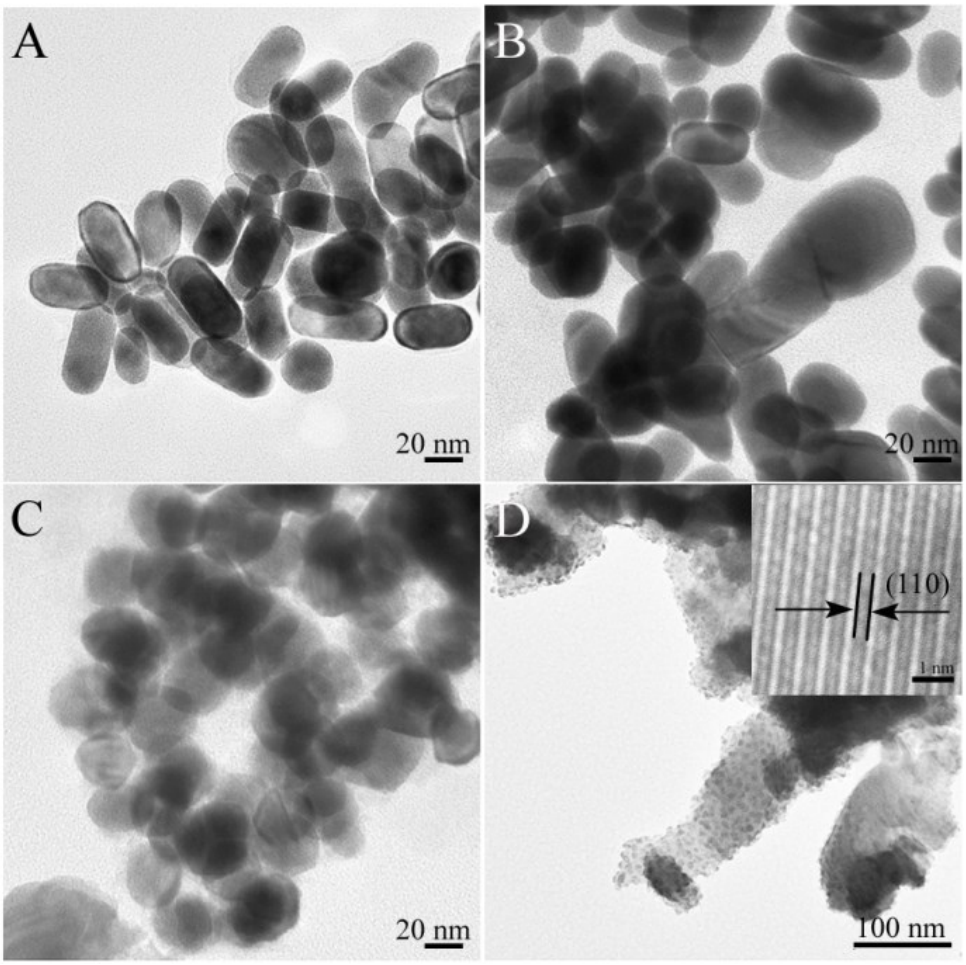

Figure 3.10. TEM images of nanoparticles synthesized by reacting CTAB stabilized gold nanorods with a 2:1 TOP/TOPO ratio. A) Nanorods and irregular shapes of gold particles were the major product at 1 h. B) Larger spherical gold particles were produced after reacting gold nanorods in TOP/TOPO for 6 h. C) A mixture of Au_2P_3 particles (low contrast particles) and gold (high contrast particles) result from the reaction of CTAB functionalized gold nanorods with TOP/TOPO (2:1 ratio) at 6 h. D) Low magnification image of Au_2P_3 "nano-networks" after reacting with a TOP/TOPO ratio of 2:1 for 10 h. After high magnification images were taken of the sample, the Au_2P_3 nanoparticles show evidence of phase separation during the TEM imaging experiments as evidenced by the dark spots of gold on the surface. Inset: TEM image of lattice fringes with lattice spacing of 5.1 Å that corresponds to (110) plane of Au_2P_3.

When the reaction was carried out for 1 h to 3 h, gold nanoparticles were obtained as the major products (Figures 3.10A & B). As can be seen in Figure 3.10C, Au_2P_3 particles were produced at 6 h (low contrast particles). It should be noted that phase separation of Au_2P_3 to gold nanoparticles was only observed at high magnification and not during low magnifications TEM imaging experiments (Figure 3.10C). After reacting CTAB functionalized gold nanorods in a 2:1 TOP/TOPO ratio for 10 h, phase pure Au_2P_3 was produced (Figure 3.10D). Analysis of the final product using TEM revealed the formation of 45 nm – 85 nm sized "nano-networks" consisting large, polydisperse crystallites (Figure 3.10D). These nanostructures exhibit distinct lattice fringes with a spacing of 5.1 Å that correspond to the (110) planes of monoclinic Au_2P_3 as shown in Figure 3.10D (inset). Gold nanoparticles present within a layer of Au_2P_3 were observed as darker high contrast regions as shown in Figure 3.10D and these uniform sized spherical particles had the average size of 7 (± 1) nm (Figure 3.10D). Figure 3.5 shows the powder XRD pattern of the same sample of Au_2P_3 shown in Figure 3.10D. Although the gold phase was not observed by XRD, TEM images clearly show the presence of gold nanoparticles. From the TEM imaging experiments it is clear that the Au_2P_3 samples undergo decomposition in the presence of the intense electron beam, forming gold nanoparticles.

3.3.4 Catalytic Activity

Phase pure Au_2P_3 "nano-networks" synthesized by reacting TOP/TOPO 2:1 ratio with CTAB functionalized gold nanorods were tested for catalytic activity towards the hydrogen evolution reaction (HER). Figure 3.11 shows the electrocatalytic activity of the gold phosphide nanoparticles tested using 0.10 M $HClO_4$ in a standard electrochemical configuration. The nanoparticles were coated onto glassy carbon working electrodes having the diameter of 5 mm and an area of 0.196 cm^2 with a loading of 50 ug/cm^2. The synthesized Au_2P_3 nanoparticles generally showed 2-3 times higher HER activities than polycrystalline Au as shown in Figure 3.11. The increase in the HER activity is probably due to the increased in the surface area of

nanoparticles instead of using a metal disk. Pt activities are provided as a reference since Pt is the typical baseline catalyst. The Nernstian diffusion limited overpotential is also given as a reference for HOR activity. As shown in Figure 3.11, the HOR activity of Pt is in line with the Nernstian diffusion limited overpotential. This indicates that we are not measuring kinetics, but the limited transport of hydrogen diffusion to and from the working electrode in HER experiments.

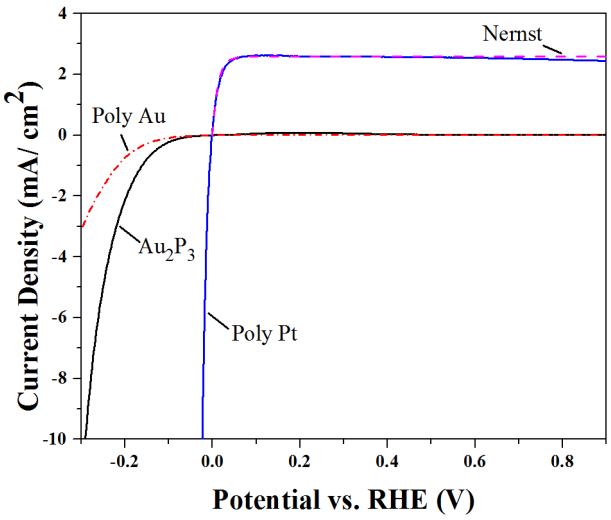

Figure 3.11. Polarization data for three Au_2P_3 electrodes in 0.1 M $HClO_4$ acid with polycrystalline gold and platinum for comparison.

The gold phosphide particles generated from CTAB functionalized gold nanoparticles ripen significantly, which reduces the surface area of the particles. Analyzing phase pure Au_2P_3 particles, pure TOPO, and TOP using FTIR showed a sharp peak at 1144 cm^{-1} corresponding to P=O stretching of TOPO or oxidized TOP which got shifted to 1096 cm^{-1}. This confirms the presence of metal bound P=O groups[98,120] on Au_2P_3 surface even after sonication and cleaning treatments (Figure 3.12), which can also lead to the reduced reactivity of the Au_2P_3. It may be possible to improve the reactivity of Au_2P_3 by reducing the size of the particles and elimination surface capping ligands.

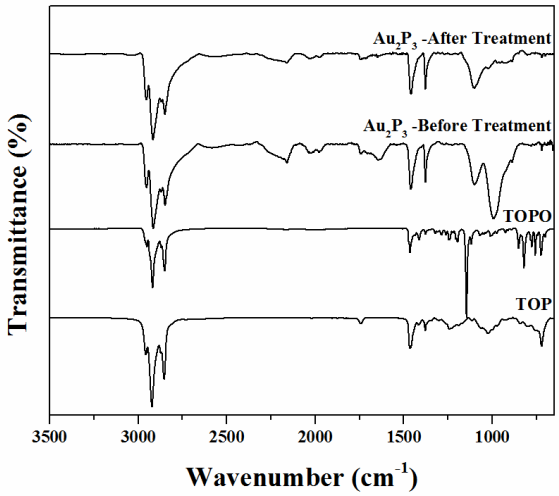

Figure 3.12. FTIR spectra of pure TOP, pure TOPO, Au_2P_3 prepared by reacting CTAB coated gold nanorods and TOP/TOPO 2:1 ratio for 10 h (Au_2P_3-Before treatment), and Au_2P_3 sample used for catalysis experiments (Au_2P_3-After treatment).

3.4. CONCLUSION

In this study, the metastable phase of gold phosphide was synthesized by reacting gold nanorods with TOP at 360 °C by generating elemental phosphorous by the thermal decomposition of TOP. Although the pre-synthesized gold nanorods were used as the templates to control the shape of the gold phosphide, gold nanorods simply act as reactants instead of templates. Results show that the gold phosphide reaction is sensitive to the surface capping agent on the gold nanorod precursors and the amount of TOP used. Increasing the TOP/TOPO to a 2:1 ratio compared to 1:1 results in higher yields of Au_2P_3 with both CTAB and 1-dodecanethiol stabilized gold nanorods. When CTAB stabilized gold nanorods were reacted with 2:1 ratio of TOP/TOPO, Au_2P_3 was generated with the highest conversion efficiency. Even though lower yields of Au_2P_3 obtained with 1-dodecanethiol functionalized gold nanorods, the thiol capping agents generated discrete particles of Au_2P_3 while reducing sintering and agglomeration. This study shows that with the choice of a carefully chosen surface stabilizer and by optimizing the reaction conditions further, it may be possible to generate Au_2P_3 particles having control over the size and shape.

Interesting, phase separation and growth of gold nanoparticles on the surface of Au_2P_3 was also observed during TEM imaging experiments. Compared to polycrystalline gold, Au_2P_3 showed higher catalytic activity for hydrogen evolution reaction. However, by controlling the size of gold phosphides particles further, an improvement on the catalytic activity is expected.

CHAPTER IV

CADMIUM SULFIDE DEPOSITION ON MICROSTRUCTURED SURFACES BY CHEMICAL BATH DEPOSITION

Note: This chapter was published in *Mater. Sci. Semicond. Process*. **2015**, *30*, 174-180. DOI: 10.1016/j.mssp.2014.10.002, and reprinted with permission.

4.1 INTRODUCTION

CdS is a direct band gap semiconductor (2.4 eV), having applications in optoelectronic devices such as photo-conducting cells, photo-sensors, transducers, laser materials, and optical wave guides and non-linear integrated optical devices.[25,121,122] Due to these applications, several synthetic methods have been developed to produce CdS that include hydrothermal,[123] electrochemical,[26] and chemical bath deposition (CBD).[124] Among these synthetic protocols, chemical bath deposition is known to be a simple and inexpensive method for the deposition of CdS on large surface areas.[125,126] In a typical chemical bath deposition process, CdS will be deposited onto the desired substrate based on the slow release of Cd^{2+} and S^{2-} ions in an aqueous alkaline conditions.[127]

Previous studies have demonstrated that both the cubic and hexagonal crystal structures of CdS films can be prepared using chemical bath deposition. Generating phase pure films and nanostructures, however, remains a challenge since variables such as temperature, pH, and

the identity of the substrate can affect the phase of the resulting film. For example, the work done by Lejmi and Savadogo[128] showed that CdS films deposited on glass substrates resulted in the prominent cubic phase (20% hexagonal and 80% cubic) when the deposition was carried out for more than 1 h in the presence of hetero-polyacids. It has also been reported that crystal structure and optical properties of CdS films can also be affected by the type of substrate used (i.e. glass, polycarbonate, polyethyleneterephthalate, and octadecyltricholorosilane functionalized silicon).[126,129]

Given the importance of the substrate on the crystal structure and the fact that textured, non-uniform substrates can be potential targets for CdS deposition, the current study was developed to test the effect of substrate topography on the uniformity and crystal structure of the CdS films deposited using CBD and also to identify the effect of microstructured surfaces on the growth of CdS as nanowires. To our knowledge, there are no current reports on the deposition of CdS using CBD on microstructured surfaces except one of the studies regarding the growth of polygonal rings and wires of CuS on microstructured surfaces *via* CBD.[29] In this work, we demonstrate both that the CBD method can be used for conformal and uniform deposition of CdS films onto patterned microstructures, and that the phase purity of CdS varies with deposition time and pH, but not necessarily with the identity of the substrate. Both the metastable cubic CdS and the high-temperature bulk hexagonal type CdS are accessible at low temperatures (85 ˚C) by varying pH on textured surfaces bearing micropillar arrays. In addition, we also demonstrated that the textured surfaces used in this study do not appear to have any effect on the nucleation or the growth of CdS as nanowires.

4.2 EXPERIMENTAL SECTION

4.2.1 Chemicals

Cadmium acetate (Cd $(CH_3COO)_2$, 98%), ammonium acetate (NH_4CH_3COO, 98%), thiourea ($SC(NH_2)_2$) and ammonium hydroxide (NH_4OH) were purchased from Sigma-Aldrich. All chemicals were used without further purification, and stock solutions were prepared using deionized water (18.2 MΩ). Dedicated glassware was used and cleaned before each reaction with aqua regia and then rinsed with deionized water. Epoxy OG-142(EPO-Technology) was used to make the epoxy substrates.

4.2.2 Preparation of Microstructured Surfaces

A Si wafer bearing an etched hexagonal array of micropillars with dimensions, d = 1 μm, l = 4 μm, and interpillar spacing d_{int} = 3 μm was used as a master mold from which the microstructures were replicated into poly (dimethyl)siloxane (PDMS) molds using soft lithography techniques as described elsewhere.[12,13] Microstructures which is present in PDMS were then replicated into epoxy by the use of UV curing and these epoxy molds were used for CdS deposition. Flat epoxy samples were also generated from PDMS molds as control samples.

4.2.3 Deposition of CdS on Microstructured Surfaces using CBD

CdS deposition methods were adapted from Oladeji and Chow.[131] Briefly, distilled water (250 mL) was heated to 85 ˚C while stirring at 400 rpm. Once distilled water reached to 85 ˚C, two substrates (25.4 mm × 76.2 mm) were dipped in the water bath and cadmium acetate (0.5 M, 1.20 mL), ammonium acetate (2.0 M, 6.00 mL), ammonium hydroxide (14.4 M, 12.16 mL) and thiourea (0.5 M, 7.00 mL) were added into the same distilled water bath. Finally, the volume of the solution was adjusted to 300 mL by adding distilled water which was pre-heated to 85 ˚C. CdS deposition was carried out for 30 min. to 240 min. while keeping the volume of the solution constant. After the desired deposition time, one substrate was air-dried and the other was sonicated in warm water for 5

min. To study the effect of pH on CdS deposition, initial pH of the solution was adjusted to pH 10 and pH 8 by varying the ammonium hydroxide concentration while having the Cd: S ratio as 1:6. The pH of the solution was also monitored throughout the reaction time and flat epoxy samples and pre-cleaned glass slides were also used as the control samples. Furthermore, to study the possibility of growing CdS nanowires on epoxy microstructured surfaces by using pillar heads as nucleating sites, Au/Pd coated epoxy and Au/Pd coated, 1-dodecanethiol functionalized epoxy microstructured surfaces were also used as substrates in CBD.

4.2.4 Characterization

All epoxy substrates, glass slides, and CdS powder was characterized using SEM (FEI Quanta 600). Bruker D8 Advance XRD was used in analyzing the crystal structures of CdS. UV-Vis absorption spectra were taken by using Cary 4E spectrophotometer and photoluminescence studies were done by using Fluorolog-3 spectrophotometer at the excitation wavelength of 420 nm. The thickness of the CdS films was also analyzed using Dektak XT profilometer.

4.3 RESULTS AND DISCUSSION

4.3.1 XRD Analysis

CdS can exist either in the thermodynamically stable hexagonal wurtzite crystal structure (WZ, $P6_3mc$) or cubic zinc-blende (ZB, $F\bar{4}3m$) structures.[132,133] At room temperature (25 ˚C) and a pressure of 1 atm, the WZ crystal phase of CdS is the most stable phase when compared to the metastable zinc-blende (ZB) crystal phase although the energy difference is only a few milli-electron volts per atom.[132] It has been reported that colloidal CdS generally exists in WZ crystal structure like bulk samples,[134] whereas, nanocrystalline CdS can form in both the WZ and the less stable ZB structure.[135] In this study, we observe that both the crystal phases of CdS (WZ and ZB crystal phase) can co-exist under the same reaction conditions depending on the pH of the solution.

Based on the time-dependent XRD data gathered by analyzing CdS films grown at pH 8 and pH 10 on micropillar arrays, flat epoxy samples and glass slides, it is clear that the crystal structure of CdS does not vary depending on type of substrate used for deposition. The same CdS crystal structure was detected in the solid particles obtained from the reaction precipitates as observed on the substrates used at both the pH values. CdS deposition was carried out at pH 8 with varying deposition time from 30 min. to 240 min. According to the XRD data obtained at pH 8, it is clear that the hexagonal crystal structure of CdS is the most prominent phase at all deposition times starting from 30 min. to 240 min. (Figure 4.1). As shown in Figure 4.1, the observation of a relatively intense (002) peak for CdS deposited at pH 8 compared to the bulk hexagonal crystal phase indicates preferential growth along the c-axis rather than random orientation.[24,133,136] At the initial reaction pH of 8, no impurities were observed that could be attributed to the cubic phase of CdS (e.g. absence of (200) cubic CdS peak). The WZ CdS phase is known to be accessible only at temperatures as high as 800 ˚C, with many groups reporting the minimum temperature for phase transition from cubic (ZB) to hexagonal (WZ) as 300 ˚C.[23] In this study, we were able to achieve phase pure WZ crystal structure of CdS at a temperature as low as 85 ˚C. This observation suggests that pH of the reaction mixture plays an important role in the decomposition kinetics of thiourea and aids in the formation of this high temperature phase at temperatures as low as 85 ˚C.

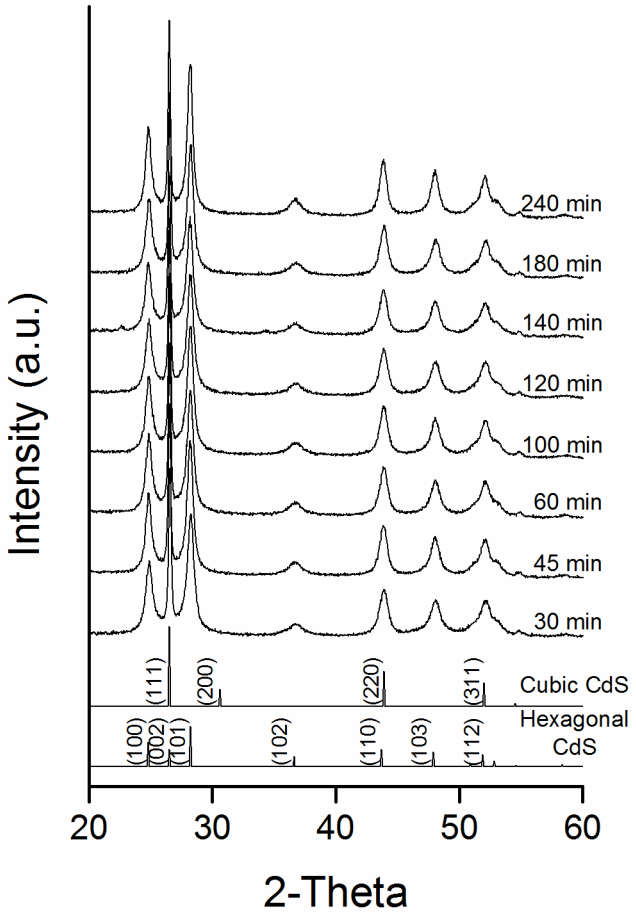

Figure 4.1. Time – dependent X-ray diffraction patterns of hexagonal (WZ-type) CdS synthesized by CBD at pH = 8. The WZ structure is dominant at all-time intervals and no impurities due to the cubic ZB structure.

Figure 4.2 shows the XRD patterns of CdS deposited at pH 10 with varying reaction time from 30 to 240 min. At an initial reaction pH of 10, the ZB crystal structure was observed on all substrates analyzed (micropillar arrays, flat epoxy samples (control), glass slides (control)), and even in solid precipitates. The presence of the (111), (220), (311) and (200) reflections of the ZB phase at 2θ values of 26.5˚, 43.9˚, and 52˚ together with a small broad peak at 32˚ can be attributed to ZB crystal structure. Some impurity peaks were also visible throughout the reaction process which could be attributed to the WZ phase of CdS. However, under the reaction

conditions used for the chemical bath deposition process, the metastable ZB structure was the most prominent phase at all deposition times. When the pH of the solution mixture was monitored, a drop of two pH units starting from pH 10 to pH 8 was observed during the 3 h deposition time. This suggests that the ammonium hydroxide equilibrium greatly influences the crystal phase and is a likely reason that the reaction results in a mixture of hexagonal and cubic crystal structures.

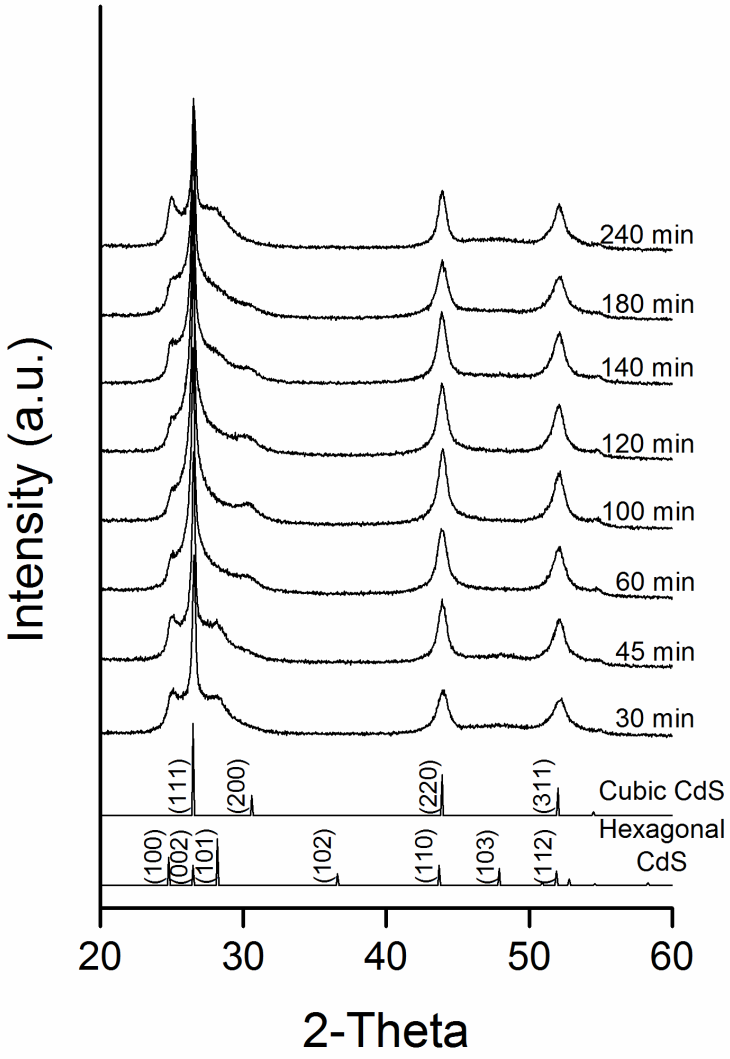

Figure 4.2. Time – dependent X-ray diffraction patterns of CdS synthesized by CBD at pH = 10. The ZB structure is dominant at all-time intervals with some impurities due to the hexagonal WZ structure.

This is consistent with the work done by Huang and workers where they observed changes in the structure of CdS thin films by varying the ammonia and ammonium acetate concentrations while affecting the pH of the reaction mixture.[136] At pH 10 when a high concentration of ammonium hydroxide is present, the equilibrium shifts towards the formation of ammonia which complexes with Cd^{2+} to form $[Cd(NH_3)_4]^{2+}$ (Eqs. (1) and (2)).[24] Previous studies have reported that the hydrolysis of thiourea (Eqs. (3a) and (3b)) is highly sensitive to the temperature, pH, and even to the catalytic effect of certain solids species and surfaces.[21] However, when a high concentration of OH^- is present in the reaction mixture the thiourea hydrolysis would take place at a fast rate producing free S^{2-} ions in the solution while decreasing the OH^- concentration. This free S^{2-} will combine with available Cd^{2+} to precipitates as CdS as shown in Eq. (4). This process shifts the thiourea equilibrium continuously to the right.[24] Since the concentration of ammonium hydroxide effects the formation of $[Cd(NH_3)_4]^{2+}$ complex (Eq. (2)), it can also affect the $Cd(OH)_2$ formation during the course of the reaction as shown in Eq. (5).

$$NH_4^+ + OH^- \leftrightarrow NH_3 + H_2O \quad (1)$$

$$Cd^{2+} + 4\ NH_3 \leftrightarrow [Cd(NH_3)_4]^{2+} \quad (2)$$

$$(NH_2)_2CS + OH^- \leftrightarrow SH^- + H_2O + H_2NCN \quad (3a)$$

$$SH^- + OH^- \leftrightarrow S^{2-} + H_2O \quad (3b)$$

$$Cd^{2+} + S^{2-} \leftrightarrow CdS \quad (4)$$

$$Cd^{2+} + 2\ OH^- \leftrightarrow Cd(OH)_2 \quad (5)$$

According to the literature, two mechanisms have been reported on the formation of CdS by chemical bath deposition: the ion-by-ion mechanism and cluster (hydroxide) mechanism. Depending on the concentration of reaction precursors, these two mechanisms can shift from one

to the other throughout the deposition process.[24] In the cluster (hydroxide) mechanism, small amounts of $Cd(OH)_2$ initially form on the substrate, and CdS forms when the OH^- groups in $Cd(OH)_2$ are replaced by S^{2-} ions. The cluster mechanism or the hydroxide mechanism can be simple as shown in Eq. (6) or it can happen via the formation of the complex (Eq. (7)) that subsequently decomposes to produce CdS.

$$Cd(OH)_2 + S^{2-} \rightarrow CdS + 2OH^- \quad (6)$$

$$Cd(OH)_2.SC(NH_2)_2 \rightarrow CdS + H_2NCN + 2H_2O \quad (7)$$

In the case of the ion-by-ion mechanism, heterogeneous nucleation of CdS would take place in the presence of a surface (substrate) where it is less likely to go through the formation of $Cd(OH)_2$. The ion-by-ion can also be categorized as simple ion-by-ion mechanism (Eq. (4)) or a complex-decomposition ion-by-ion mechanism (Eqs. (8a) & (8b)).

$$Cd^{2+} + (NH_2)_2CS \leftrightarrow [(NH_2)_2CS\text{-}Cd]^{2+} \quad (8a)$$

$$[(NH_2)_2CS\text{-}Cd]^{2+} + 2OH^- \rightarrow CdS + H_2NCN + 2H_2O \quad (8b)$$

Based on the results obtained at pH 10, the cubic (ZB) crystal structure was observed as the prominent phase. At basic pH, with the faster hydrolysis of thiourea and controlled release of Cd^{2+}, both the cluster mechanism and the ion-by-ion mechanism can occur simultaneously leading to a mixture of crystal structures. At high pH, since $Cd(OH)_2$ can form on the substrate surface, the cluster (hydroxide) mechanism is favored which leads to a prominent cubic phase.

At pH 8, S^{2-} ions are not released in considerable amounts, due to the slow decomposition of thiourea at a low concentration of OH^-. Therefore, it is less likely undergo the cluster mechanism forming $Cd(OH)_2$.[24,137] Since the ion-by-ion mechanism is favored over the cluster mechanism, a prominent hexagonal phase is observed at pH 8. In addition, impurities of the hexagonal phase are observed when the experiment is carried out at pH=10 as the pH decreases

over time to approximately pH 8, which again provides evidence that pH affects the formation of the crystal structure.

4.3.2 SEM Analysis

Figure 4.3 shows the SEM images of CdS thin films deposited on the epoxy surfaces at pH 10 with varying deposition time.

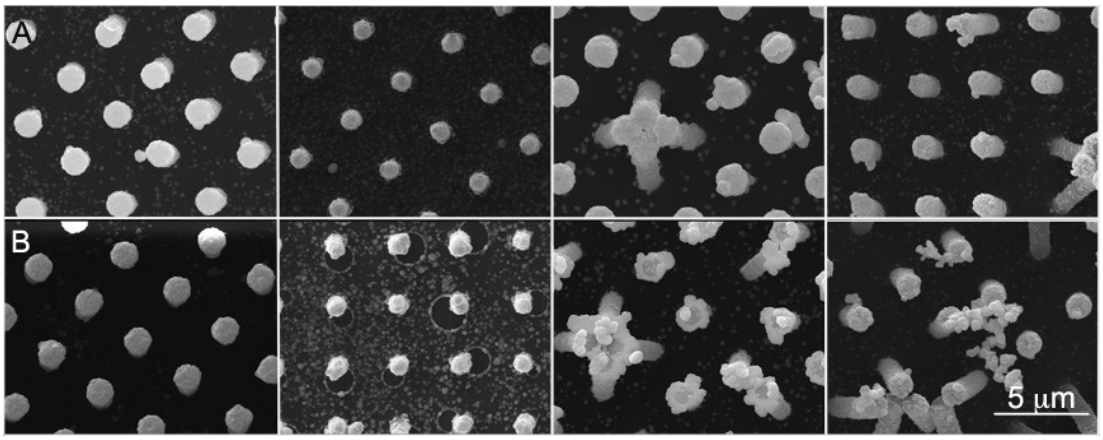

Figure 4.3. SEM images of CdS thin films deposited on a hexagonal array of epoxy micropillars synthesized by CBD at pH = 10. A) SEM images of as deposited CdS thin films at 30 min., 100 min., 180 min., and 240 min. (from left to right). B) SEM images of epoxy micropillar arrays with CdS thin film at 30 min., 100 min., 180 min., and 240 min. (from left to right) after sonication (5 min.). The micropillar array samples form densely packed aggregates at shorter times (below 100 min.) and flower-like structures, or network-like structures at longer deposition times (above 180 min.).

According to the SEM analysis, compact and conformal thin films of CdS were observed on the micropillars having granular-like morphology (Figure 4.3A). The formation of these compact aggregates is probably due to the faster hydrolysis of thiourea at pH 10 that leads to a high deposition rate. The integrity of the films on the micropillar arrays was not affected by sonication as shown in Figure 4.3B. At longer deposition times, flat flower- like structures were also observed on the tips of the micropillars in some samples (Figure 4.3, 180 min.). Together

with these different morphologies, small colloidal particles of CdS were also observed at the bottom surface of the epoxy micropillar substrate.

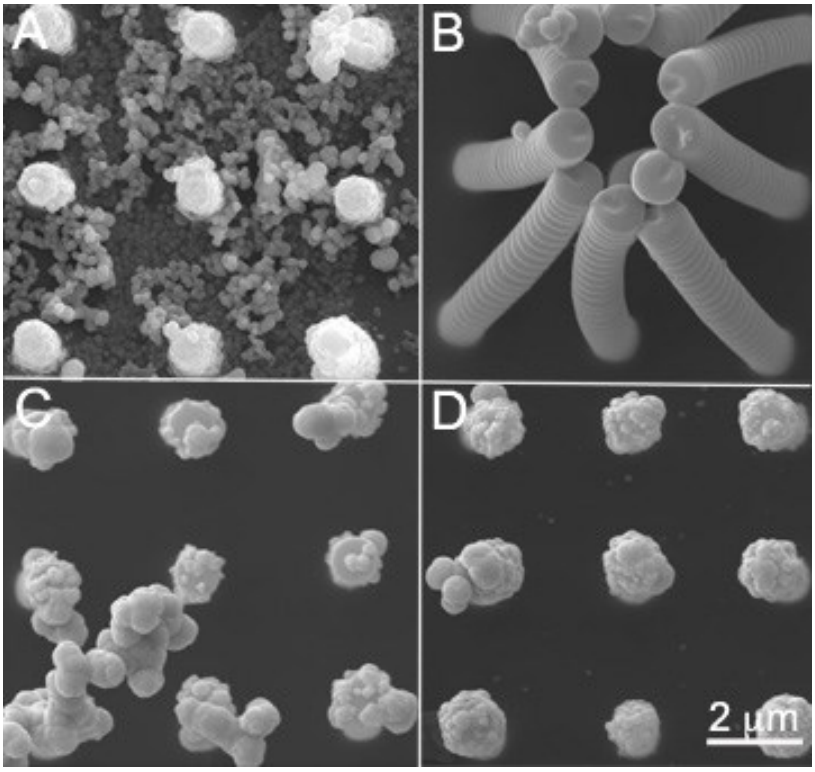

Figure 4.4. SEM images of CdS thin films deposited on a hexagonal array of epoxy micropillars synthesized by CBD at pH = 8 after sonication at A) 30 min., B) 100 min., C) 180 min., and D) 240 min. At 30 min., a large number of aggregates are observed at the bottom surface of the micropillar array substrate. This may be due to CdS aggregates formed in solution, that loosely deposit on the surface. Conformal CdS films are observed at deposition times at 100 min. with the ridges of the epoxy microstructures uniformly coated. Clustering of the micropillars can occur as a result of the drying process that produces capillary forces between the structures. Aggregates can also nucleate (C and D) at the surface of the microstructures at longer deposition times (180-240 min.), which can form network-like structures and that connect neighboring pillars.

Figure 4.4 demonstrates representative SEM images of CdS films deposited on the micropillar arrays at pH 8 from 30 - 240 min. Aggregates and precipitates of CdS were observed for some samples at 30 min. This could be due to the more fragile adhesion of the CdS film to the micropillars at short deposition times, which makes the films more susceptible to sonication and stirring (Figure 4.4A). However, with longer deposition times, a uniform and a conformal layer of

CdS is observed for all samples. Figure 4.4B shows a side view of the micropillar structures with tiny ridges having uniformly coated CdS film. Clustering of micropillars that can be seen in Figure 4.4B, which is probably due to the capillary forces formed as the aqueous solution dries from between the microstructures. This can be avoided with careful sample handling and by using slow drying process. Beyond 180 min., the tips of the pillars act as nucleating sites that result in the formation of the "web-like" and "network-like" structures of CdS that start to grow from the tips of the pillars (Figures 4.4C & 4.4D). These nano growths were formed by the fusion of spherical CdS clusters that grow and connect neighboring pillars (Figure 4.4D) which are consistent with the ion-by-ion mechanism.

4.3.3 Optical Properties

The UV-Vis absorption spectra of CdS thin films deposited on glass slides at pH 10 and pH 8 are shown in Figure 4.5A. The absorption onset and the band gap values of the samples were determined from the peak minimum values of the first derivative of the respective absorbance plots. The absorption onset values and band gap calculated for thin films deposited at pH 8 and pH 10 are given in Table 4.1. Slight blue shifting in the absorption spectra was observed for both CdS thin films deposited at pH 10 and pH 8, compared to the bulk value. This could be attributed to smaller and polydisperse crystallite size of CdS particles deposited on the films.

To further calculate the particle size of CdS in thin films deposited at pH 10 and pH 8, effective mass approximation (EMA) (Eq. (9)) was used, which relates the particle size, d, and the band gap E_g for particles larger than 4 nm.[138]

$$E_g = E_g(0) + \alpha / d^{\beta} \qquad (9)$$

where $E_g(0)$ is the band gap of the bulk hexagonal CdS (2.42 eV), and α and β are constants. According to the experimental fitting data taken from Lippens and Lannoo, this α and β were

determined as 13 eV.nm^2 and 2 respectively.[139] Based on the calculations, thin films deposited at pH 8 consisted of particles with smaller crystallite size (13 nm) compared to thin films deposited at pH 10 (20 nm) providing further evidence that the ion-by-ion mechanism is likely dominant at pH 8.

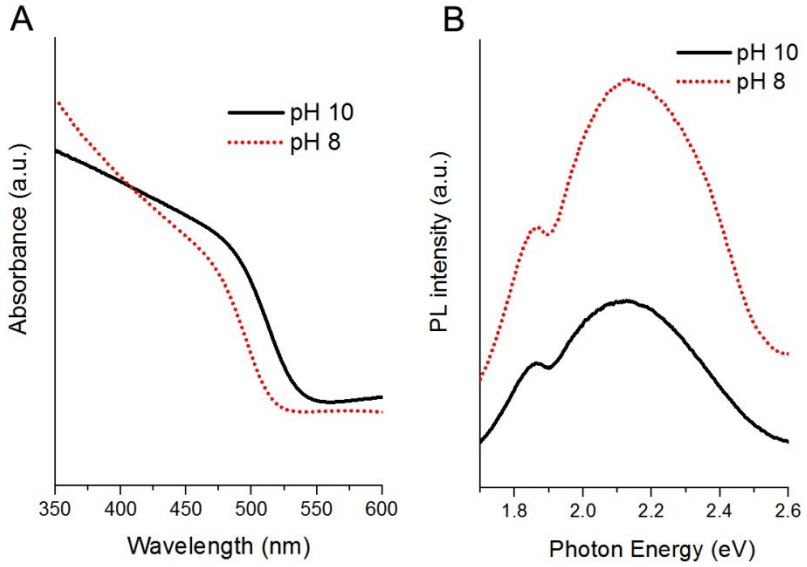

Figure 4.5. Representative A) UV-Vis and B) photoluminescence spectra of CdS thin films deposited at pH 8 and pH 10 (180 min).

Table 4.1. Average absorption onset values, band gaps determined using UV-Vis absorption spectra of CdS thin films deposited at pH 8 and pH 10 and estimated particle size of respective CdS thin films using effective mass approximation.

	Absorption onset value (nm)	**Band gap (eV)**	**Particle size of the CdS in the thin film (nm)**
pH 8	499	2.49	13
pH 10	507	2.45	20

4.3.4 Photoluminescence Properties

Photoluminescence (PL) spectroscopy of the CdS films on the glass substrates was performed at room temperature (Figure 4.5B) at an excitation of 420 nm. The samples were yellow in color but transitioned over time to a darker yellow-orange color for both pH 8 and pH 10 experiments (for both glass and epoxy substrates). WZ and ZB type CdS thin films had emission spectra dominated by a broad peak between 2.10 eV to 2.13 eV known as the "yellow band" that arises from interstitial Cd or S vacancies.[27,125] A less intense peak at 1. 87 eV, commonly referred to as the "red band," was also observed which has been attributed to sulfur vacancies in radiative recombination. The broad emission spectra are likely to contain bands in the "orange" (2.07-2.18 eV) due to donor-acceptor recombination and "green" (2.18-2.54 eV) associated with deep donor-states to the valence band (WZ to ZB phase transformation).[140-142] The PL spectra are consistent with other CdS films grown *via* CBD with little difference between WZ and ZB phases.[27,143,144] A more intense "red band" observed in our samples is likely due to higher levels of interstitial Cd or S vacancies as a result of excess thiourea used in our reaction conditions. However, a more detailed temperature dependent study is necessary to further interpret the spectra.

4.3.5 Effect of Epoxy Substrate on the Growth of CdS as Nanowires

To identify the possibility of growing nanowires of CdS using pillar heads of microstructured surfaces as the nucleating sites, epoxy substrates with micropillars were coated with Au/Pd and functionalized with 1-dodecanethiol to promote the adhesion of CdS particles. When Au/Pd coated epoxy microstructured surfaces were used as the substrates for chemical bath deposition at pH 10 by varying the deposition time, thin films of CdS was observed covering the pillars (Figure 4.6).

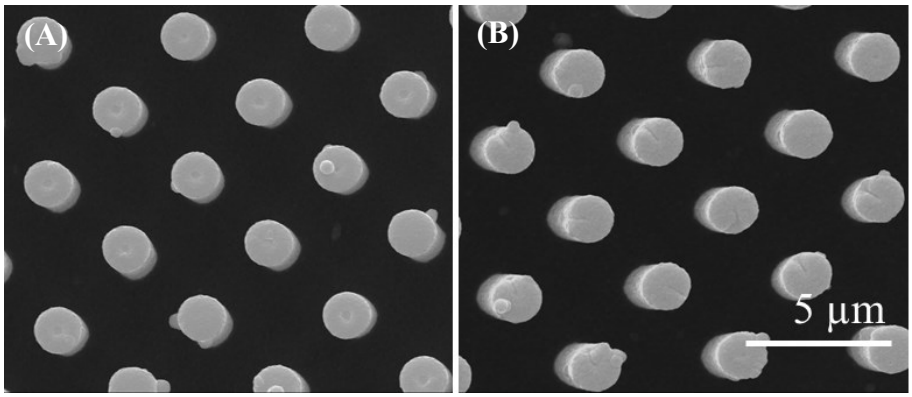

Figure 4.6. SEM images of CdS thin films deposited on an Au/Pd coated hexagonal array of epoxy micropillars synthesized by CBD at pH 10 for 180 min. A) Unwashed and B) Sonicated samples. Thin films of CdS were observed on the micropillars.

When Au/Pd coated epoxy surfaces were further functionalized with 1-dodecanethiol, small outgrowths of CdS were observed on the tips of the pillars at 3 h of deposition time (Figure 4.7a) which grew into short, chain-like structures at 6 h. With the longer deposition times (10 h), long CdS nanowires were seen in some places of the epoxy substrate as shown in Figure 4.7c. However, compared to the previous studies done with CuS, CdS showed a lower propensity to grow as long nanowires when using micropillar heads as the nucleating sites.

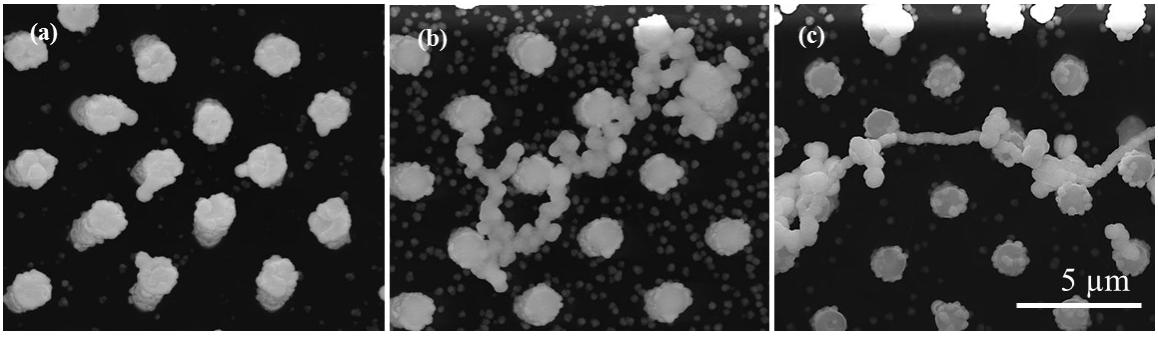

Figure 4.7. SEM images of CdS deposited at pH 10 on 1-dodecanethiol functionalized, Au/Pd coated epoxy substrates having micropillars by varying the deposition time to 3 h (a), 6 h (b) and 10 h (c).

4.4 CONCLUSION

Chemical bath deposition can be used for the conformal deposition of CdS films on non-uniform surfaces such as micropillar arrays with dimensions as small as d = 1 μm and h = 4 μm. It was demonstrated that both the ZB and WZ crystal structures of CdS are accessible by varying the pH of the chemical bath. When a large excess of thiourea is present, both the cluster mechanism and the ion-by-ion mechanism can occur, which results in the possibility of obtaining either the ZB or WZ crystal structure. pH plays two major roles including affecting the decomposition kinetics of thiourea as well affecting the Cd^{2+}- complex formation. The cluster (hydroxide) mechanism is favored at pH = 10 since $Cd(OH)_2$ can form on the surface of the substrate that leads to a prominent cubic phase. The ion-by-ion mechanism is likely favored at pH = 8 and results in the hexagonal phase of CdS. Deposition of CdS on the micropillar surfaces is uniform and conformal with the formation of packed clusters on the micropillars at pH 10 that form flower-like structures at long deposition times. Smaller crystallites are observed on micropillar arrays at pH 8 with “net-work” like structures observed at long deposition times. This work suggests that the crystal structure of CdS and phase purity can be controlled by maintaining the pH of the CBD reaction constant at pH = 10 for cubic and pH = 8 for hexagonal crystal structure.

CHAPTER V

SUMMURY AND CONCLUSIONS

Chapter II highlights interactions of gold nanorods with HeLa cells in terms of cell viability and cellular uptake. Gold nanorods with different aspect ratios were synthesized using seed-mediated method and effect of surface functionalization on the cellular uptake. The toxicity was also studied by functionalizing the CTAB coated gold nanorods with mPEG molecules. Studies demonstrated that the cell viability depends on the chemical composition of the supernatant, especially the free CTAB and the aspect ratio of gold nanorod does not have any effect. Cellular uptake studies of different aspect ratios of gold nanorods did not show significant differences from aspect ratio 2.6 to 5.4. However, with aspect ratio 11.5, HeLa cells showed higher cellular uptake compared to the shorter aspect ratios analyzed. Taken together, it is clear that not just the aspect ratio plays an important role in cellular uptake of nanorods, the synthesis protocols, functionalization and purification processes also have a major effect on cellular uptake. Observations of higher uptake for AR 11.5 Au nanorods having CTAB as the surface coating,

proves the positive effect of CTAB on cellular uptake, although the free CTAB is toxic to the cells.In chapter III the metastable phase of gold phosphide was synthesized by reacting gold nanorods with TOP. Although the pre-synthesized gold nanorods were used to template the size and shape to the resulting gold phosphide, gold nanorods simply acted as reactants instead of morphological templates. Our results highlighted that the gold phosphide reaction is sensitive to the surface capping agent and the TOP/TOPO ratio used. Higher yields Au_2P_3 were obtained with both CTAB and 1-dodecanethiol stabilized gold nanorods with increased amounts of TOP/TOPO ratio. Use of weak surface stabilizer such as CTAB on gold nanorods surface exhibited higher conversion to gold phosphide. Even though lower yields of Au_2P_3 were obtained with 1-dodecanethiol functionalized gold nanorods, the thiol capping agents generated discrete particles of Au_2P_3 while reducing sintering and agglomeration. Phase separation and growth of gold nanoparticles on the surface of Au_2P_3 was also observed during TEM imaging experiments. During hydrogen evolution reaction (HER) experiments, higher catalytic activity was observed with Au_2P_3 compared to polycrystalline gold. However, by controlling the size of gold phosphides particles further and eliminating surface capping agents, an improvement on the catalytic activity is expected.

In chapter IV, the effect substrate topography in obtaining different morphologies and crystal structures of CdS has been studied. This work demonstrated the possibility of obtaining both the ZB and WZ crystal structures of CdS by varying the pH of the chemical bath. pH plays two important roles affecting the decomposition kinetics of thiourea as well affecting the Cd^{2+}-complex formation, which can further affect the deposition mechanism of CdS. At pH = 10 when the cluster (hydroxide) mechanism is favored prominent cubic phase was observed while forming packed clusters on the micropillars and flower-like structures at long deposition times. In contrast, at the pH=8 pure hexagonal phase of CdS was observed due to the presence of ion-by-ion mechanism at lower pH and smaller crystallites are observed on micropillar arrays with the

formation of “net-work” like structures at long deposition times. This work suggests that the crystal structure of CdS and phase purity can be controlled by maintaining the pH of the chemical bath.

REFERENCES

(1) Bhushan, B. *Springer handbook of nanotechnology*; Springer Science & Business Media, 2010.

(2) Maynard, A. D.; Aitken, R. J.; Butz, T.; Colvin, V.; Donaldson, K.; Oberdorster, G.; Philbert, M. A.; Ryan, J.; Seaton, A.; Stone, V.; Tinkle, S. S.; Tran, L.; Walker, N. J.; Warheit, D. B. Safe handling of nanotechnology. *Nature* **2006**, *444*, 267-269.

(3) Wang, X.; Song, J.; Wang, Z. L. Nanowire and nanobelt arrays of zinc oxide from synthesis to properties and to novel devices. *J. Mater. Chem.* **2007**, *17*, 711-720.

(4) Karthick, B.; Maheshwari, R. Lotus-inspired nanotechnology applications. *Resonance* **2008**, *13*, 1141-1145.

(5) Kralj, S.; Makovec, D. Magnetic assembly of superparamagnetic iron oxide nanoparticle clusters into nanochains and nanobundles. *ACS Nano* **2015**, *9*, 9700-9707.

(6) Lu, W.; Lieber, C. M. Nanoelectronics from the bottom up. *Nature materials* **2007**, *6*, 841-850.

(7) Biswas, A.; Bayer, I. S.; Biris, A. S.; Wang, T.; Dervishi, E.; Faupel, F. Advances in top–down and bottom–up surface nanofabrication: Techniques, applications & future prospects. *Adv. Colloid Interface Sci.* **2012**, *170*, 2-27.

(8) Monge, M.; Kahn, M. L.; Maisonnat, A.; Chaudret, B. Room-temperature organometallic synthesis of soluble and crystalline zno nanoparticles of controlled size and shape. *Angew. Chem. Int. Ed.* **2003**, *42*, 5321-5324.

(9) Carpenter, M. K.; Moylan, T. E.; Kukreja, R. S.; Atwan, M. H.; Tessema, M. M. Solvothermal synthesis of platinum alloy nanoparticles for oxygen reduction electrocatalysis. *J. Am. Chem. Soc.* **2012**, *134*, 8535-8542.

(10) Yang, Y.; Matsubara, S.; Xiong, L.; Hayakawa, T.; Nogami, M. Solvothermal synthesis of multiple shapes of silver nanoparticles and their SERS properties. *J. Phys. Chem. C* **2007**, *111*, 9095-9104.

(11) Murphy, C. J.; Sau, T. K.; Gole, A. M.; Orendorff, C. J.; Gao, J.; Gou, L.; Hunyadi, S. E.; Li, T. Anisotropic metal nanoparticles: synthesis, assembly, and optical applications. *J. Phys. Chem. B* **2005**, *109 (29)*, 13857–13870.

(12) Grzelczak, M.; Pérez-Juste, J.; Mulvaney, P.; Liz-Marzán, L. M. Shape control in gold nanoparticle synthesis. *Chem. Soc. Rev.* **2008**, *37*, 1783-1791.

(13) Ferraz, M.; Monteiro, F.; Manuel, C. Hydroxyapatite nanoparticles: a review of preparation methodologies. *J. Appl. Biom. Biom.* **2004**, *2*, 74-80.

(14) Maaz, K.; Karim, S.; Mumtaz, A.; Hasanain, S.; Liu, J.; Duan, J. Synthesis and magnetic characterization of nickel ferrite nanoparticles prepared by co-precipitation route. *J. Magn. Magn. Mater.* **2009**, *321*, 1838-1842.

(15) Kim, D.; Zhang, Y.; Voit, W.; Rao, K.; Muhammed, M. Synthesis and characterization of surfactant-coated superparamagnetic monodispersed iron oxide nanoparticles. *J. Magn. Magn. Mater.* **2001**, *225*, 30-36.

(16) Huang, X.; Neretina, S.; El-Sayed, M. A. Gold nanorods: from synthesis and properties to biological and biomedical applications. *Adv. Mater.* **2009**, *21*, 4880-4910.

(17) Wang, L.; Liu, Y.; Li, W.; Jiang, X.; Ji, Y.; Wu, X.; Xu, L.; Qiu, Y.; Zhao, K.; Wei, T.; Li, Y.; Zhao, Y.; Chen, C. Selective targeting of gold nanorods at the mitochondria of cancer cells: implications for cancer therapy. *Nano Lett.* **2011**, *11*, 772-780.

(18) Murphy, C. J.; Sau, T. K.; Gole, A. M.; Orendorff, C. J.; Gao, J.; Gou, L.; Hunyadi, S. E.; Li, T. Anisotropic metal nanoparticles: synthesis, assembly, and optical applications. *J. Phys. Chem. B* **2005**, *109*, 13857-13870.

(19) Murphy, C. J.; Thompson, L. B.; Alkilany, A. M.; Sisco, P. N.; Boulos, S. P.; Sivapalan, S. T.; Yang, J. A.; Chernak, D. J.; Huang, J. The many faces of gold nanorods. *J. Phys. Chem. Lett.* **2010**, *1*, 2867-2875.

(20) Qiu, Y.; Liu, Y.; Wang, L.; Xu, L.; Bai, R.; Ji, Y.; Wu, X.; Zhao, Y.; Li, Y.; Chen, C. Surface chemistry and aspect ratio mediated cellular uptake of Au nanorods. *Biomaterials* **2010**, *31*, 7606-7619.

(21) Yang, H.; Chen, Z.; Zhang, L.; Yung, W.-Y.; Leung, K. C.-F.; Chan, H. Y. E.; Choi, C. H. J. Mechanism for the cellular uptake of targeted gold nanorods of defined aspect ratios. *Small* **2016**, *12*, 5178-5189.

(22) Chithrani, B. D.; Ghazani, A. A.; Chan, W. C. W. Determining the size and shape dependence of gold nanoparticle uptake into mammalian cells. *Nano Lett.* **2006**, *6*, 662-668.

(23) Pawar, S. M.; Pawar, B. S.; Kim, J. H.; Joo, O.-S.; Lokhande, C. D. Recent status of chemical bath deposited metal chalcogenide and metal oxide thin films. *Curr. Appl. Phys.* **2011**, *11*, 117-161.

(24) Hodes, G. *Chemical solution deposition of semiconductor films*; CRC press, 2002.

(25) Pham, L. Q.; Van, T.-K.; Cha, H. G.; Kang, Y. S. Controlling crystal growth orientation and crystallinity of cadmium sulfide nanocrystals in aqueous phase by using cationic surfactant. *CrystEngComm* **2012**, *14*, 7888-7890.

(26) Şişman, İ.; Alanyalıoğlu, M.; Demir, Ü. Atom-by-atom growth of cds thin films by an electrochemical co-deposition method: effects of ph on the growth mechanism and structure. *J. Phys. Chem. C* **2007**, *111*, 2670-2674.

(27) Moon, B.-S.; Lee, J.-H.; Jung, H. Comparative studies of the properties of CdS films deposited on different substrates by R.F. sputtering. *Thin Solid Films* **2006**, *511*, 299-303.

(28) Hadia, N. M. A.; Garcia-Granda, S.; Garcia, J. R. Characterization of single crystalline CdS nanowires synthesized by solvothermal method. *J. Nanosci. Nanotechnol.* **2014**, *14*, 5449-5454.

(29) Vasquez, Y.; Fenton, E. M.; Chernow, V. F.; Aizenberg, J. Growth of polygonal rings and wires of CuS on structured surfaces. *CrystEngComm* **2011**, *13*, 1077-1080.

(30) Islam, M. A.; Hossain, M. S.; Aliyu, M. M.; Chelvanathan, P.; Huda, Q.; Karim, M. R.; Sopian, K.; Amin, N. Comparison of structural and optical properties of cds thin films grown by CSVT, CBD and sputtering techniques. *Energy Procedia* **2013**, *33*, 203-213.

(31) Choy, K.; Su, B. Growth behavior and microstructure of CdS thin films deposited by an electrostatic spray assisted vapor deposition (ESAVD) process. *Thin Solid Films* **2001**, *388*, 9-14.

(32) Carenco, S.; Portehault, D.; Boissière, C.; Mézailles, N.; Sanchez, C. Nanoscaled metal borides and phosphides: recent developments and perspectives. *Chem. Rev.* **2013**, *113*, 7981-8065.

(33) Wang, X.; Kolen'ko, Y. V.; Bao, X. Q.; Kovnir, K.; Liu, L. One-step synthesis of self-supported nickel phosphide nanosheet array cathodes for efficient electrocatalytic hydrogen generation. *Angew. Chem. Int. Ed.* **2015**, *54*, 8188-8192.

(34) Ni, Y.; Tao, A.; Hu, G.; Cao, X.; Wei, X.; Yang, Z. Synthesis, characterization and properties of hollow nickel phosphide nanospheres. *Nanotechnology* **2006**, *17*, 5013.

(35) Jin, H.; Uenishi, J.; Christ, W. J.; Kishi, Y. Catalytic effect of nickel (II) chloride and palladium (II) acetate on chromium (II)-mediated coupling reaction of iodo olefins with aldehydes. *J. Am. Chem. Soc.* **1986**, *108*, 5644-5646.

(36) Wang, J.; Johnston-Peck, A. C.; Tracy, J. B. Nickel phosphide nanoparticles with hollow, solid, and amorphous structures. *Chem. Mater.* **2009**, *21*, 4462-4467.

(37) Popczun, E. J.; Read, C. G.; Roske, C. W.; Lewis, N. S.; Schaak, R. E. Highly active electrocatalysis of the hydrogen evolution reaction by cobalt phosphide nanoparticles. *Angew. Chem.* **2014**, *126*, 5531-5534.

(38) Callejas, J. F.; McEnaney, J. M.; Read, C. G.; Crompton, J. C.; Biacchi, A. J.; Popczun, E. J.; Gordon, T. R.; Lewis, N. S.; Schaak, R. E. Electrocatalytic and photocatalytic hydrogen production from acidic and neutral-pH aqueous solutions using iron phosphide nanoparticles. *ACS nano* **2014**, *8*, 11101-11107.

(39) Subramanian, V.; Wolf, E. E.; Kamat, P. V. Catalysis with TiO_2/gold nanocomposites. Effect of metal particle size on the Fermi level equilibration. *J. Am. Chem. Soc.* **2004**, *126*, 4943-4950.

(40) Valden, M.; Lai, X.; Goodman, D. W. Onset of catalytic activity of gold clusters on titania with the appearance of nonmetallic properties. *science* **1998**, *281*, 1647-1650.

(41) Haruta, M. Size-and support-dependency in the catalysis of gold. *Catal. Today* **1997**, *36*, 153-166.

(42) Haruta, M. Catalysis of gold nanoparticles deposited on metal oxides. *Cattech* **2002**, *6*, 102-115.

(43) Layek, K.; Kantam, M. L.; Shirai, M.; Nishio-Hamane, D.; Sasaki, T.; Maheswaran, H. Gold nanoparticles stabilized on nanocrystalline magnesium oxide as an active catalyst for reduction of nitroarenes in aqueous medium at room temperature. *Green chemistry* **2012**, *14*, 3164-3174.

(44) Murphy, C. J.; Gole, A. M.; Stone, J. W.; Sisco, P. N.; Alkilany, A. M.; Goldsmith, E. C.; Baxter, S. C. Gold nanoparticles in biology: beyond toxicity to cellular imaging. *Acc. Chem. Res.* **2008**, *41*, 1721-1730.

(45) Huang, X.; Neretina, S.; El-Sayed, M. A. Gold nanorods: from synthesis and properties to biological and biomedical applications. *Adv. Mater.* **2009**, *21*, 4880-4910.

(46) Xiao, J.; Qi, L. Surfactant-assisted, shape-controlled synthesis of gold nanocrystals. *Nanoscale* **2011**, *3*, 1383-1396.

(47) Carnovale, C.; Bryant, G.; Shukla, R.; Bansal, V. Size, shape and surface chemistry of nano-gold dictate its cellular interactions, uptake and toxicity. *Prog. Mater Sci.* **2016**, *83*, 152-190.

(48) Gaser, N. A.; Raffaella, M.; Silvia, D.; Marta, d. A.; Marco Scotto, d. A.; Teresa, P.; Alberto, D. PEGylated gold nanorods as optical trackers for biomedical applications: an in vivo and in vitro comparative study. *Nanotechnology* **2016**, *27*, 255101.

(49) Hornyak, G. L.; Patrissi, C. J.; Martin, C. R. Fabrication, characterization, and optical properties of gold nanoparticle/porous alumina composites: the nonscattering maxwell−garnett limit. *J. Phys. Chem. B* **1997**, *101*, 1548-1555.

(50) Yu; Chang, S.-S.; Lee, C.-L.; Wang, C. R. C. Gold nanorods: electrochemical synthesis and optical properties. *J. Phys. Chem. B* **1997**, *101*, 6661-6664.

(51) Sau, T. K.; Murphy, C. J. Seeded high yield synthesis of short au nanorods in aqueous solution. *Langmuir* **2004**, *20*, 6414-6420.

(52) Park, W. M.; Huh, Y. S.; Hong, W. H. Aspect-ratio-controlled synthesis of high-aspect-ratio gold nanorods in high-yield. *Curr. Appl. Phys.* **2009**, *9*, e140-e143.

(53) Nikoobakht, B.; El-Sayed, M. A. Preparation and growth mechanism of gold nanorods (NRs) using seed-mediated growth method. *Chem. Mater.* **2003**, *15*, 1957-1962.

(54) Wilhelm, S.; Tavares, A. J.; Dai, Q.; Ohta, S.; Audet, J.; Dvorak, H. F.; Chan, W. C. W. Analysis of nanoparticle delivery to tumours. *Nat. Rev. Mater.* **2016**, *1*, 16014.

(55) Grabinski, C.; Schaeublin, N.; Wijaya, A.; D'Couto, H.; Baxamusa, S. H.; Hamad-Schifferli, K.; Hussain, S. M. Effect of gold nanorod surface chemistry on cellular response. *ACS Nano* **2011**, *5*, 2870-2879.

(56) Zarska, M.; Novotny, F.; Havel, F.; Sramek, M.; Babelova, A.; Benada, O.; Novotny, M.; Saran, H.; Kuca, K.; Musilek, K.; Hvezdova, Z.; Dzijak, R.; Vancurova, M.; Krejcikova, K.; Gabajova, B.; Hanzlikova, H.; Kyjacova, L.; Bartek, J.; Proska, J.; Hodny, Z. Two-step mechanism of cellular uptake of cationic gold nanoparticles modified by (16-mercaptohexadecyl)trimethylammonium bromide. *Bioconjugate Chem.* **2016**, *27*, 2558-2574.

(57) Chithrani, B. D.; Chan, W. C. W. Elucidating the mechanism of cellular uptake and removal of protein-coated gold nanoparticles of different sizes and shapes. *Nano Lett.* **2007**, *7*, 1542-1550.

(58) Arnida; Malugin, A.; Ghandehari, H. Cellular uptake and toxicity of gold nanoparticles in prostate cancer cells: a comparative study of rods and spheres. *J. Appl. Toxicol.* **2010**, *30*, 212-217.

(59) Vigderman, L.; Zubarev, E. R. High-yield synthesis of gold nanorods with longitudinal spr peak greater than 1200 nm using hydroquinone as a reducing agent. *Chem. Mater.* **2013**, *25*, 1450-1457.

(60) Busbee, B. D.; Obare, S. O.; Murphy, C. J. An improved synthesis of high-aspect-ratio gold nanorods. *Adv. Mater.* **2003**, *15*, 414-416.

(61) Vigderman, L.; Manna, P.; Zubarev, E. R. Quantitative replacement of cetyl trimethylammonium bromide by cationic thiol ligands on the surface of gold nanorods and their extremely large uptake by cancer cells. *Angew. Chem.* **2012**, *124*, 660-665.

(62) Orendorff, C. J.; Murphy, C. J. Quantitation of metal content in the silver-assisted growth of gold nanorods. *J. Phys. Chem. B* **2006**, *110*, 3990-3994.

(63) Zhang, Z.; Lin, M. Fast loading of PEG-SH on CTAB-protected gold nanorods. *RSC Advances* **2014**, *4*, 17760-17767.

(64) Boca, S. C.; Astilean, S. Detoxification of gold nanorods by conjugation with thiolated poly (ethylene glycol) and their assessment as SERS-active carriers of Raman tags. *Nanotechnology* **2010**, *21*, 235601.

(65) Alkilany, A. M.; Nagaria, P. K.; Hexel, C. R.; Shaw, T. J.; Murphy, C. J.; Wyatt, M. D. Cellular uptake and cytotoxicity of gold nanorods: molecular origin of cytotoxicity and surface effects. *Small* **2009**, *5*, 701-708.

(66) Wang, L.; Li, J.; Pan, J.; Jiang, X.; Ji, Y.; Li, Y.; Qu, Y.; Zhao, Y.; Wu, X.; Chen, C. Revealing the binding structure of the protein corona on gold nanorods using synchrotron radiation-based techniques: understanding the reduced damage in cell membranes. *J. Am. Chem. Soc.* **2013**, *135*, 17359-17368.

(67) Zhang, S.; Gao, H.; Bao, G. Physical principles of nanoparticle cellular endocytosis. *ACS nano* **2015**, *9*, 8655-8671.

(68) Michel, R.; Pasche, S.; Textor, M.; Castner, D. G. The influence of PEG architecture on protein adsorption and conformation. *Langmuir* **2005**, *21*, 12327-12332.

(69) Gui, C.; Cui, D.-x. Functionalized gold nanorods for tumor imaging and targeted therapy. *Cancer Biology & Medicine* **2012**, *9*, 221-233.

(70) Hauck, T. S.; Ghazani, A. A.; Chan, W. C. W. Assessing the effect of surface chemistry on gold nanorod uptake, toxicity, and gene expression in mammalian cells. *Small* **2008**, *4*, 153-159.

(71) Lesniak, A.; Salvati, A.; Santos-Martinez, M. J.; Radomski, M. W.; Dawson, K. A.; Åberg, C. Nanoparticle adhesion to the cell membrane and its effect on nanoparticle uptake efficiency. *J. Am. Chem. Soc.* **2013**, *135*, 1438-1444.

(72) Cho, E. C.; Zhang, Q.; Xia, Y. The effect of sedimentation and diffusion on cellular uptake of gold nanoparticles. *Nature nanotechnology* **2011**, *6*, 385-391.

(73) Huang, C.; Zhang, Y.; Yuan, H.; Gao, H.; Zhang, S. Role of nanoparticle geometry in endocytosis: laying down to stand up. *Nano Lett.* **2013**, *13*, 4546-4550.

(74) Souza, D. C. S.; Pralong, V.; Jacobson, A. J.; Nazar, L. F. A reversible solid-state crystalline transformation in a metal phosphide induced by redox chemistry. *Science* **2002**, *296*, 2012-2015.

(75) Yang, R.; Chueh, Y.-L.; Morber, J. R.; Snyder, R.; Chou, L.-J.; Wang, Z. L. Single-crystalline branched zinc phosphide nanostructures: synthesis, properties, and optoelectronic devices. *Nano Lett.* **2007**, *7*, 269-275.

(76) Brock, S. L.; Perera, S. C.; Stamm, K. L. Chemical routes for production of transition-metal phosphides on the nanoscale: implications for advanced magnetic and catalytic materials. *Chem – Eur. J.***2004**, *10*, 3364-3371.

(77) Popczun, E. J.; McKone, J. R.; Read, C. G.; Biacchi, A. J.; Wiltrout, A. M.; Lewis, N. S.; Schaak, R. E. Nanostructured nickel phosphide as an electrocatalyst for the hydrogen evolution reaction. *J. Am. Chem. Soc.* **2013**, *135*, 9267-9270.

(78) Saadi, F. H.; Carim, A. I.; Verlage, E.; Hemminger, J. C.; Lewis, N. S.; Soriaga, M. P. CoP as an Acid-stable active electrocatalyst for the hydrogen-evolution reaction: electrochemical synthesis, interfacial characterization and performance evaluation. *J. Phys. Chem. C* **2014**, *118*, 29294-29300.

(79) Popczun, E. J.; Read, C. G.; Roske, C. W.; Lewis, N. S.; Schaak, R. E. Highly active electrocatalysis of the hydrogen evolution reaction by cobalt phosphide nanoparticles. *Angew. Chem. Int. Ed.* **2014**, *53*, 5427-5430.

(80) Xiao, P.; Sk, M. A.; Thia, L.; Ge, X.; Lim, R. J.; Wang, J.-Y.; Lim, K. H.; Wang, X. Molybdenum phosphide as an efficient electrocatalyst for the hydrogen evolution reaction. *Energy Environ. Sci.* **2014**, *7*, 2624-2629.

(81) Xu, Y.; Wu, R.; Zhang, J.; Shi, Y.; Zhang, B. Anion-exchange synthesis of nanoporous FeP nanosheets as electrocatalysts for hydrogen evolution reaction. *Chem. Commun.* **2013**, *49*, 6656-6658.

(82) Tian, J.; Liu, Q.; Asiri, A. M.; Sun, X. Self-supported nanoporous cobalt phosphide nanowire arrays: an efficient 3d hydrogen-evolving cathode over the wide range of pH 0–14. *J. Am. Chem. Soc.* **2014**, *136*, 7587-7590.

(83) McEnaney, J. M.; Crompton, J. C.; Callejas, J. F.; Popczun, E. J.; Biacchi, A. J.; Lewis, N. S.; Schaak, R. E. Amorphous molybdenum phosphide nanoparticles for electrocatalytic hydrogen evolution. *Chem. Mater.* **2014**, *26*, 4826-4831.

(84) Abu, I. I.; Smith, K. J. The effect of cobalt addition to bulk MoP and Ni_2P catalysts for the hydrodesulfurization of 4,6-dimethyldibenzothiophene. *J. Catal.* **2006**, *241*, 356-366.

(85) Bando, K. K.; Wada, T.; Miyamoto, T.; Miyazaki, K.; Takakusagi, S.; Koike, Y.; Inada, Y.; Nomura, M.; Yamaguchi, A.; Gott, T.; Ted Oyama, S.; Asakura, K. Combined in situ QXAFS and FTIR analysis of a Ni phosphide catalyst under hydrodesulfurization conditions. *J. Catal.* **2012**, *286*, 165-171.

(86) Burns, A. W.; Gaudette, A. F.; Bussell, M. E. Hydrodesulfurization properties of cobalt–nickel phosphide catalysts: Ni-rich materials are highly active. *J. Catal.* **2008**, *260*, 262-269.

(87) Eijsbouts, S.; Mayo, S. W.; Fujita, K. Unsupported transition metal sulfide catalysts: from fundamentals to industrial application. *Appl. Catal. A Gen.* **2007**, *322*, 58-66.

(88) Gaudette, A. F.; Burns, A. W.; Hayes, J. R.; Smith, M. C.; Bowker, R. H.; Seda, T.; Bussell, M. E. Mössbauer spectroscopy investigation and hydrodesulfurization properties of iron–nickel phosphide catalysts. *J. Catal.* **2010**, *272*, 18-27.

(89) Guan, Q.; Sun, C.; Li, R.; Li, W. The synthesis and investigation of ruthenium phosphide catalysts. *Catal. Commun.* **2011**, *14*, 114-117.

(90) Hayes, J. R.; Bowker, R. H.; Gaudette, A. F.; Smith, M. C.; Moak, C. E.; Nam, C. Y.; Pratum, T. K.; Bussell, M. E. Hydrodesulfurization properties of rhodium phosphide: Comparison with rhodium metal and sulfide catalysts. *J. Catal.* **2010**, *276*, 249-258.

(91) Kanda, Y.; Temma, C.; Nakata, K.; Kobayashi, T.; Sugioka, M.; Uemichi, Y. Preparation and performance of noble metal phosphides supported on silica as new hydrodesulfurization catalysts. *Appl. Catal. A Gen.* **2010**, *386*, 171-178.

(92) Layan Savithra, G. H.; Bowker, R. H.; Carrillo, B. A.; Bussell, M. E.; Brock, S. L. Mesoporous matrix encapsulation for the synthesis of monodisperse Pd_5P_2 nanoparticle hydrodesulfurization catalysts. *ACS Appl. Mater. Interfaces* **2013**, *5*, 5403-5407.

(93) Oyama, S. T.; Lee, Y.-K. The active site of nickel phosphide catalysts for the hydrodesulfurization of 4,6-DMDBT. *J. Catal.* **2008**, *258*, 393-400.

(94) Oyama, S. T.; Gott, T.; Zhao, H.; Lee, Y.-K. Transition metal phosphide hydroprocessing catalysts: A review. *Catal. Today* **2009**, *143*, 94-107.

(95) Sawhill, S. J.; Layman, K. A.; Van Wyk, D. R.; Engelhard, M. H.; Wang, C.; Bussell, M. E. Thiophene hydrodesulfurization over nickel phosphide catalysts: effect of the precursor composition and support. *J. Catal.* **2005**, *231*, 300-313.

(96) Stinner, C.; Prins, R.; Weber, T. Binary and ternary transition-metal phosphides as HDN catalysts. *J. Catal.* **2001**, *202*, 187-194.

(97) Sun, F.; Wu, W.; Wu, Z.; Guo, J.; Wei, Z.; Yang, Y.; Jiang, Z.; Tian, F.; Li, C. Dibenzothiophene hydrodesulfurization activity and surface sites of silica-supported MoP, Ni_2P, and NiMoP catalysts. *J. Catal.* **2004**, *228*, 298-310.

(98) Senevirathne, K.; Burns, A. W.; Bussell, M. E.; Brock, S. L. Synthesis and characterization of discrete nickel phosphide nanoparticles: effect of surface ligation chemistry on catalytic hydrodesulfurization of thiophene. *Adv. Funct. Mater.* **2007**, *17*, 3933-3939.

(99) Panneerselvam, A.; Malik, M. A.; Afzaal, M.; O'Brien, P.; Helliwell, M. The chemical vapor deposition of nickel phosphide or selenide thin films from a single precursor. *J. Am. Chem. Soc.* **2008**, *130*, 2420-2421.

(100) Stamm, K. L.; Garno, J. C.; Liu, G.-y.; Brock, S. L. A General methodology for the synthesis of transition metal pnictide nanoparticles from pnictate precursors and its application to iron−phosphorus phases. *J. Am. Chem. Soc.* **2003**, *125*, 4038-4039.

(101) Perera, S. C.; Fodor, P. S.; Tsoi, G. M.; Wenger, L. E.; Brock, S. L. Application of de-silylation strategies to the preparation of transition metal pnictide nanocrystals: the case of FeP. *Chem. Mater.* **2003**, *15*, 4034-4038.

(102) Xie, Y.; Su, H. L.; Qian, X. F.; Liu, X. M.; Qian, Y. T. A Mild one-step solvothermal route to metal phosphides (metal=Co, Ni, Cu). *J. Solid State Chem.* **2000**, *149*, 88-91.

(103) Henkes, A. E.; Vasquez, Y.; Schaak, R. E. Converting metals into phosphides: a general strategy for the synthesis of metal phosphide nanocrystals. *J. Am. Chem. Soc.* **2007**, *129*, 1896-1897.

(104) Henkes, A. E.; Schaak, R. E. Trioctylphosphine: A general phosphorus source for the low-temperature conversion of metals into metal phosphides. *Chem. Mater.* **2007**, *19*, 4234-4242.

(105) Lukehart, C. M.; Milne, S. B.; Stock, S. R. Formation of crystalline nanoclusters of Fe_2P, RuP, Co_2P, Rh_2P, Ni_2P, Pd_5P_2, or PtP_2 in a silica xerogel matrix from single-source molecular precursors. *Chem. Mater.* **1998**, *10*, 903-908.

(106) Maneeprakorn, W.; Malik, M. A.; O'Brien, P. The preparation of cobalt phosphide and cobalt chalcogenide (CoX, X = S, Se) nanoparticles from single source precursors. *J. Mater. Chem.* **2010**, *20*, 2329-2335.

(107) Kelly, A. T.; Rusakova, I.; Ould-Ely, T.; Hofmann, C.; Lüttge, A.; Whitmire, K. H. Iron phosphide nanostructures produced from a single-source

organometallic precursor: nanorods, bundles, crosses, and spherulites. *Nano Lett.* **2007**, *7*, 2920-2925.

(108) Chiang, R.-K.; Chiang, R.-T. Formation of hollow Ni_2P nanoparticles based on the nanoscale kirkendall effect. *Inorg. Chem.* **2007**, *46*, 369-371.

(109) Layan Savithra, G. H.; Muthuswamy, E.; Bowker, R. H.; Carrillo, B. A.; Bussell, M. E.; Brock, S. L. Rational design of nickel phosphide hydrodesulfurization catalysts: controlling particle size and preventing sintering. *Chem. Mater.* **2013**, *25*, 825-833.

(110) Luber, E. J.; Mobarok, M. H.; Buriak, J. M. Solution-processed zinc phosphide (α-Zn_3P_2) colloidal semiconducting nanocrystals for thin film photovoltaic applications. *ACS Nano* **2013**, *7*, 8136-8146.

(111) Fatemi, N. S.; Weizer, V. G. The formation of low resistance electrical contacts to shallow junction InP devices without compromising emitter integrity. *J. Electron. Mater.* **1991**, *20*, 875-880.

(112) Baker, A.; Usher, F. L. Nuclear gold sols. II. Mechanism of formation. *Trans. Faraday Soc.* **1940**, *35*, 385-392.

(113) Carenco, S.; Florea, I.; Ersen, O.; Boissiere, C.; Mezailles, N.; Sanchez, C. Towards nanoscaled gold phosphides: surface passivation and growth of composite nanostructures. *New J. Chem.* **2013**, *37*, 1231-1237.

(114) Schaak, R. E.; Sra, A. K.; Leonard, B. M.; Cable, R. E.; Bauer, J. C.; Han, Y.-F.; Means, J.; Teizer, W.; Vasquez, Y.; Funck, E. S. Metallurgy in a beaker:

nanoparticle toolkit for the rapid low-temperature solution synthesis of functional multimetallic solid-state materials. *J. Am. Chem. Soc.* **2005**, *127*, 3506-3515.

(115) Vasquez, Y.; Luo, Z.; Schaak, R. E. Low-temperature solution synthesis of the non-equilibrium ordered intermetallic compounds Au_3Fe, Au_3Co, and Au_3Ni as Nanocrystals. *J. Am. Chem. Soc.* **2008**, *130*, 11866-11867.

(116) Vasquez, Y.; Henkes, A. E.; Chris Bauer, J.; Schaak, R. E. Nanocrystal conversion chemistry: A unified and materials-general strategy for the template-based synthesis of nanocrystalline solids. *J. Solid State Chem.* **2008**, *181*, 1509-1523.

(117) Stoeva, S.; Klabunde, K. J.; Sorensen, C. M.; Dragieva, I. Gram-scale synthesis of monodisperse gold colloids by the solvated metal atom dispersion method and digestive ripening and their organization into two- and three-dimensional structures. *J. Am. Chem. Soc.* **2002**, *124*, 2305-2311.

(118) Prasad, B. L. V.; Stoeva, S. I.; Sorensen, C. M.; Klabunde, K. J. Digestive ripening of thiolated gold nanoparticles: the effect of alkyl chain length. *Langmuir* **2002**, *18*, 7515-7520.

(119) Prasad, B. L. V.; Stoeva, S. I.; Sorensen, C. M.; Klabunde, K. J. Digestive-ripening agents for gold nanoparticles: alternatives to thiols. *Chem. Mater.* **2003**, *15*, 935-942.

(120) Ghatak, A.; Debnath, G. H.; Mandal, M.; Mukherjee, P. Lanthanide cation-induced tuning of surface capping properties in zinc sulfide nanoparticles: an infrared absorption study. *RSC Advances* **2015**, *5*, 32920-32932.

(121) Yang, Z. X.; Zhong, W.; Zhang, P.; Xu, M. H.; Deng, Y.; Au, C. T.; Du, Y. W. Controllable synthesis, characterization and photoluminescence properties of morphology-tunable CdS nanomaterials generated in thermal evaporation processes. *Appl. Surf. Sci.* **2012**, *258*, 7343-7347.

(122) Sedaghat, Z.; Taghavinia, N.; Marandi, M. Thermal control of the size and crystalline phase of CdS nanoparticles. *Nanotechnology* **2006**, *17*, 3812.

(123) Wang, X.; Feng, Z.; Fan, D.; Fan, F.; Li, C. Shape-controlled synthesis of cds nanostructures via a solvothermal method. *Crystal Growth & Design* **2010**, *10*, 5312-5318.

(124) O'Brien, P.; Saeed, T. Deposition and characterization of cadmium sulfide thin films by chemical bath deposition. *J. Cryst. Growth* **1996**, *158*, 497-504.

(125) Cortes, A.; Gómez, H.; Marotti, R. E.; Riveros, G.; Dalchiele, E. A. Grain size dependence of the bandgap in chemical bath deposited CdS thin films. *Sol. Energy Mater. Sol. Cells* **2004**, *82*, 21-34.

(126) Lee, J.-H. Influence of substrates on the structural and optical properties of chemically deposited CdS films. *Thin Solid Films* **2007**, *515*, 6089-6093.

(127) Khallaf, H.; Oladeji, I. O.; Chai, G.; Chow, L. Characterization of CdS thin films grown by chemical bath deposition using four different cadmium sources. *Thin Solid Films* **2008**, *516*, 7306-7312.

(128) Lejmi, N.; Savadogo, O. The effect of heteropolyacids and isopolyacids on the properties of chemically bath deposited CdS thin films. *Sol. Energy Mater. Sol. Cells* **2001**, *70*, 71-83.

(129) Hwang, Y. K.; Woo, S. Y.; Lee, J. H.; Jung, D.-Y.; Kwon, Y.-U. Micropatterned CdS thin films by selective solution deposition using microcontact printing techniques. *Chem. Mater.* **2000**, *12*, 2059-2063.

(130) Pokroy, B.; Epstein, A. K.; Persson-Gulda, M. C. M.; Aizenberg, J. Fabrication of bioinspired actuated nanostructures with arbitrary geometry and stiffness. *Adv. Mater.* **2009**, *21*, 463-469.

(131) Oladeji, I. O.; Chow, L. Optimization of chemical bath deposited cadmium sulfide thin films. *J. Electrochem. Soc.* **1997**, *144*, 2342-2346.

(132) Shanavas, K. V.; Sharma, S. M.; Dasgupta, I.; Nag, A.; Hazarika, A.; Sarma, D. D. First-principles study of the effect of organic ligands on the crystal structure of cds nanoparticles. *J. Phys. Chem. C* **2012**, *116*, 6507-6511.

(133) Vemuri, R. S.; Gullapalli, S. K.; Zubia, D.; McClure, J. C.; Ramana, C. V. Structural and chemical properties of highly oriented cadmium sulfide (CdS) cauliflower films. *Chem. Phys. Lett.* **2010**, *495*, 232-235.

(134) Nag, A.; Hazarika, A.; Shanavas, K. V.; Sharma, S. M.; Dasgupta, I.; Sarma, D. D. Crystal structure engineering by fine-tuning the surface energy: the case of CdE (E = S/Se) nanocrystals. *J. Phys. Chem. Lett.* **2011**, *2*, 706-712.

(135) Martín-Rodríguez, R.; González, J.; Valiente, R.; Aguado, F.; Santamaría-Pérez, D.; Rodríguez, F. Reversibility of the zinc-blende to rock-salt phase transition in cadmium sulfide nanocrystals. *J. Appl. Phys.* **2012**, *111*, 063516.

(136) Liu, Q. Q.; Shi, J. H.; Li, Z. Q.; Zhang, D. W.; Li, X. D.; Sun, Z.; Zhang, L. Y.; Huang, S. M. Morphological and stoichiometric study of chemical bath deposited CdS films by varying ammonia concentration. *Physica B Condens. Matter* **2010**, *405*, 4360-4365.

(137) Rieke, P. C.; Bentjen, S. B. Deposition of cadmium sulfide films by decomposition of thiourea in basic solutions. *Chem. Mater.* **1993**, *5*, 43-53.

(138) Murakoshi, K.; Hosokawa, H.; Saitoh, M.; Wada, Y.; Sakata, T.; Mori, H.; Satoh, M.; Yanagida, S. Preparation of size-controlled hexagonal CdS nanocrystallites and the characteristics of their surface structures. *J. Chem. Soc., Faraday Trans.* **1998**, *94*, 579-586.

(139) Lippens, P. E.; Lannoo, M. Calculation of the band gap for small CdS and ZnS crystallites. *Phys. Rev. B* **1989**, *39*, 10935-10942.

(140) Abken, A. E.; Halliday, D. P.; Durose, K. Photoluminescence study of polycrystalline photovoltaic CdS thin film layers grown by close-spaced sublimation and chemical bath deposition. *J. Appl. Phys.* **2009**, *105*, 064515.

(141) Lozada-Morales, R.; Zelaya-Angel, O. Photoluminescence analysis of CdS thin films under phase transition. *Thin Solid Films* **1996**, *281*, 386-389.

(142) Kulp, B. A. Displacement of the cadmium atom in single crystal CdS by electron bombardment. *Phys. Rev.* **1962**, *125*, 1865-1869.

(143) Ravindran, T. R.; Arora, A. K.; Balamurugan, B.; Mehta, B. R. Inhomogeneous broadening in the photoluminescence spectrum of CdS nanoparticles. *Nanostruct. Mater.* **1999**, *11*, 603-609.

(144) Vigil, O.; Riech, I.; Garcia-Rocha, M.; Zelaya-Angel, O. Characterization of defect levels in chemically deposited CdS films in the cubic-to-hexagonal phase transition. *J. Vac. Sci. Technol. A* **1997**, *15*, 2282-2286.

VITA

Kachchakaduge Deshani Gihanthika Fernando

Candidate for the Degree of

Doctor of Philosophy

Thesis: SYNTHETIC STRATEGIES FOR GENERATING INORGANIC NANOPARTICLES WITH OPTICAL, CATALYTIC, AND BIOLOGICAL IMPORTANCE

Major Field: Chemistry

Biographical:

Education:

Completed the requirements for the Doctor of Philosophy in Chemistry at Oklahoma State University, Stillwater, Oklahoma in December, 2017.

Completed the requirements for the Bachelor of Science in Chemistry at University of Kelaniya, Kelaniya, Sri Lanka in 2009.

Experience:

Graduate Research/ Teaching Assistant (Year 2012- 2017)
Oklahoma State University, Stillwater, Oklahoma, USA.

Research Scientist (Year 2010- 2012)
Sri Lanka Institute of Nanotechnology, Sri Lanka.

Teaching Assistant (Year 2009- 2010)
Department of Chemistry, University of Kelaniya, Sri Lanka.

Professional Memberships:

Member of the Honor Society of Phi Kappa Phi (2014 – Present)
Member of the American Chemical Society (2014 – Present)
Member of the Sri Lanka Association for the Advancement of Science (2009)